STUDIES OF NOVEL GRAPHENE NANORIBBON/ POLYANILINE NANOCOMPOSITES FOR THEIR APPLICATIONS IN SOLAR CELLS

By

ASEFA ABADI DESTA

A THESIS SUBMITTED IN PARTIAL FULFILMENT OF THE REQUIREMENT FOR THE DEGREE OF MASTER OF SCIENCE IN MATERIALS SCIENCE AT ADDIS ABABA UNIVERSITY SCHOOL OF GRADUATE STUDIES

ADDIS ABABA, ETHIOPIA

MARCH 2012

ADDIS ABABA UNIVERSITY

GRADUATE STUDIES

STUDIES OF NOVEL GRAPHENE NANORIBBON/ POLYANILINE NANOCOMPOSITES FOR THEIR APPLICATIONS IN SOLAR CELLS

By: Asefa Abadi

Materials Science Program

College of Natural Science

Approved by the Examining Board

Prof. Javed Mazher
(Advisor) _____

Prof. Teketel Yohannes
(Examiner, Chairperson) _____

Dr. Gebremedhen G/Yesus
(Examiner) _____

Acknowledgment

First and for most, I would like to praise the name of the Almighty God for giving me health, patient and courage from the starting of this program till now. My gratitude also goes to my supervisor Prof. Javed Mazher, for all of his help and guidance, his critical reading, commitment, knowledge, encouragement, suggestions and constructive criticisms in the research and development of this thesis work. Sincere appreciation goes to Prof. Teketel Yohannes, the Chair of the Materials science program, for his willingness to support me in different aspects especially by providing me books. My friends also deserve a special acknowledgment for their significant contributions to this work directly or indirectly.

Finally, I wish to express my warmest thanks to my parents, sisters and brothers for their patience, moral supports, understanding and direct help in innumerable ways during the last two years.

Table of Contents

List of Tables

List of Figures

Abstract

Organic polymer nanocomposites blended with graphene nanostructures have recently attracted lot of scientific interest due to their novel heterojunction charge transport properties and for fabrication of solar cells with enhanced energy conversion efficiencies. Simulational studies of electronic and transport properties of polyaniline-graphene nanoribbon (PAn-GNR) nanocomposite systems have been performed in various conformations and in strict percolation regime. Ab-initio DFT-LDA-NEGF simulations have been carried out for at least seven compositionally vivid samples of the PAn-GNR system with built-in two-probe device geometries. As obtained density of states (DOS) and transmission spectra [T(E)] plots are examined for the charge transport behavior in these nano-systems. We have observed significant number of contributing states driven from contact electrodes in to the nanomaterial, which are described on the basis of Fano effects and as induced strong couplings. We have also studied electron and hole eigenstate conduction channels along with I–V measurements using Landauer relations for these nanocomposites which help in understanding different modes of the charge transport. For some of the samples we have observed a negative differential resistance (NDR) phenomenon which is rightly explained. Diagnoses of the NDR phenomena in respect to presence of Fano states and other DOS and transmission singularities have been conceded. Prospects of self-aligned PAN-GNR nanocomposites for solar cell applications have also discussed. The present study of nano devices would be helpful in understanding intrinsic properties of photovoltaic materials in nano-devices for their futuristic deployment in nano-solar cells.

CHAPTER ONE

1. Introduction

Graphene–aniline nano-composites are well known charge transfer systems in which the graphene accepts the charge carriers from donor aniline [1]. Recent experiments have shown that the graphene nanostructructures can be easily dissolved in aniline without any prior chemical functionalization. Such a graphene nanostructure-aniline solution can then be easily followed by the simple electropolymerization step to prepare thin films of graphene–polyaniline (Gr–PAn) nanocomposite on various conducting electrodes of preference like transparent conducting glasses, ITO (indium tin oxide), etc [1, 2]. As prepared nanocomposite thin films can be directly used in variety of applications assorting from electrochemical sensing electrode material to the bulk heterojunction (BHJ) solar cells. The wonder material graphene which is a new allotrope among the carbon based nanomaterials, has already been applied for fabricating the composites with conducting polymers [3, 4]. As the graphene, carbon nanotubes and fullerenes (C-60) have similar structure with ring symmetry, hence the conjugated graphene sheets can be readily functionalized via non-covalent π stacking or covalent C–C coupling reactions with graphene nanostructures through the formation of donor–acceptor complex within the graphene plane [5]. Hence in principle, the graphene should be the same good electron acceptor as carbon nanotubes or C-60, while aromatic amine like aniline is a fairly good electron donor and these donor type aromatic molecules can be π–π stacked on the graphene surface or edges. Thus graphene and polyaniline form a first-rate charge-transfer complex [1, 6]. Recently it has also been reported that the graphene voluntarily accepts electrons at very fast charge transfer rates, the photoinduced charge transfer rate in between organic aromatic donor to graphene was found to be 32 ps from quenched fluorescence decay life-time experiments [7]. The authors therein also explored the possibility of multiple electron transfer to the graphene when attached with sulfonated zinc phthalocyanine. Nevertheless the graphene-aniline charge transfer complex has some shortcomings also which arise from the optical absorption band of aniline which is experimentally found to be in UV range at wavelengths of 234 nm, 255 nm and 287 nm [6, 7], however for the polymers of aniline it goes down up to 350 nm which corresponds to blue absorption depending upon the monomer chain lengths [8]. Hence, the charge transfer material in its pure form is unable to absorb the low energy photonic range of a solar spectrum, this also marks the necessity of the proper light harvesting to increase the BHJ solar cell efficiencies.

Nevertheless, the wide band gap of polyaniline which varies from 1.8 eV to 3.5 eV is still a problem in achieving device efficiencies due to absorption of only shorter photonic wavelengths [8]. Apart from this, a high resistance of the PAn composites is still a major bottleneck in realizing their efficient BHJ devices due to resistive energy losses among the as-harvested charge carriers [9]. Conversely, on preparing the nano-composites of PAn with long ribbons of graphene in which the polymers are well-aligned with the ribbons by π–π stacking and are percolating throughout the composite material can reasonably improvise the scenario of their electrical properties. Hence it is a high time to address these pertaining issues especially in the context of nano-photovoltaic devices, where either due to the small size induced quantum confined transport effects or due to π–π stacking functionalization the electrical properties of these devices will change drastically. One of the aims of this thesis is to propose a scheme of smart photovoltaic materials for their deployment as the efficient light harvesters in the BHJ nanosolar cells and to simulate various electronic and transport properties of their two probe devices in which the as modeled test percolating two component nano-systems are sandwiched in between the conducting electrodes.

1.1 Organic Photovoltaic Technology

Photovoltaics (PV) technology offers a most direct way to convert solar radiation into electricity and is based on the photovoltaic effect, which was first observed by Henri Becquerel 172 years ago [10]. The photovoltaic effect is a basic physical process through which a photovoltaic cell converts sunlight into electricity. The PV technology basically involves direct conversion of solar radiation into electricity without any mechanical moving parts, any noise, high temperatures or any pollution. Apart from these benefits a series of solar or PV cells also exhibit very long lifetime. Hence it works virtually by only using the enormous energy source, the SUN, which is absolutely free, ubiquitous, inexhaustible and a very flexible energy source. One can generate huge amount of solar power ranging from microwatts to megawatts. PV cells are generally classified into three generations which indicate the order in which each become important. The vast majority of solar cells on the market are single-junction silicon wafer devices including single crystal and multicrystalline silicon, which are known as first generation solar cells [11]. Their main drawback is associated with their indirect optical band gap that requires a thick active layer for the solar conversion and thus the devices entail a costly fabrication of large

area materials. Thin-film photovoltaic technologies [12] are referred to as a second-generation photovoltaics, they are based on inorganic semiconductor materials that are more photon absorbing (solar radiation harvesting) than a crystalline silicon and thus can be processed directly onto large area substrates. Such semiconductors include amorphous silicon, II–VI semiconductors or chalcogenides such as CdS or CdTe, $CuInSe_2$ (CIS), $CuInGaSe_2$ (CIGS), etc. On the other hand, more recent organic-based approaches do not rely on conventional single p–n junctions and they are often referred to as a third generation solar technology. Various attempts to develop the third generation cells exist, such as multi-junction cells, intermediate-band cells, hot carrier cells, and bulk hetero-junction (BHJ) organic cells [13]. Categorically, the third generation photovoltaic cells include: (i) the dye-sensitized solar cells pioneered by Grätzel, which are electrochemical cells that require use of electrolytes; (ii) multijunction tendom cells fabricated from group IV and III– V semiconductor multilayers; (iii) an alternative hybrid approach, in which inorganic quantum dots are doped into a semiconducting polymer matrix or by combining nanostructured inorganic semiconductors such as TiO_2 with organic materials; (iv) lastly, all-organic solid-state approach, which is now a days a thrust area of research because of the emphasis on Green and environmentally friendly technologies [11–14]. Typical Organic photovoltaic (OPV) cells are basic thin film structures in which the organic photoactive materials are sandwiched in between two electrodes as active or photon harvesting layers. They have also attracted much attention in recent years due to their advantages in low-cost manufacturing, light weight and good flexibility [15–17]. These advantages have created great interest and thus a great deal of research work is currently being devoted to increase their power conversion efficiencies and scale-up production processes [17, 18]. However, the power conversion efficiency of organic photovoltaic cells is still low compared to their inorganic counterparts. At present a significant number of research endeavors are dedicated to enhance the efficiency of organic photovoltaic cells such as improving the work function of the electrode with different surface treatments or by incorporating other organic dopants as a hole or electron transporting layer along with inserting a buffer layer between the electrode (or hole) electron transporting layer [18].

In this section we are intended to give a brief survey of OPVs which are derived from the use of one or more components based on π-conjugated (semiconducting) organic molecules, oligomers or polymers. These OPVs show excitonic PV features due to their fabrication from a

combination of electron-donor (D) and acceptor (A) materials with suitable redox energy levels when they are sandwiched as an ultra thin film in between metallic electrodes [19]. The energy conversion process often has at least five fundamental steps [19, 20] which are as follows:

1) Photons are absorbed in the donor and excitons are created.
2) Excitons diffuse within the donor (acceptor) phase.
3) Excitons encounter an interface with the acceptor (donor) before decaying, and fast dissociation takes place, leading to charge generation and separation.
4) As separated charge carriers are transported through the various percolated nanocomposite components to the electrodes via diffusion and/or drift processes.
5) The charge carriers are collected at the electrodes.

These steps ensure that a higher non-equilibrium conductivity of photovoltaic materials will yield higher values of a charge transfer and its collection at the electrodes, obviously which will facilitate more power generation from the solar cells. At present almost all efficient OPV cells are based on the donor-acceptor (DA) heterojunction (HJ) type structure which is first demonstrated by Tang in 1986 [21]. Separately two other OPV devices are single layer and bilayer heterojunction devices. The former device consists of a semiconducting polymer layer which is sandwiched between two metal electrodes with different work functions and its functioning can be described by the metal-insulator-metal (MIM) model. The second device consists of a donor and acceptor layers where the polymer is applied with an electron acceptor layer on top, normally C-60. Such an arrangement easily facilitates lower recombination rate of the electron and hole in comparison to forward charge transport which is a necessary requirement of PV power generation. Identically in the device one can also obtain an efficient charge separation because once the exciton gets dissociated, which is by and large happens at the interface, the electrons travel towards the acceptor and the holes travel towards the donor material resulting in hefty photo-carrier generation. Since typical diffusion lengths of exciton are in the range of 10 nm while the film thickness should be more than 100 nm in order to absorb most of the light: this limits the efficiency of above mentioned device. This difficulty has been overcome by using the new concept of bulk heterojunction [22].

1.1.1 Bulk hetrojunction solar cells

Solar cells constructed of organic materials are becoming increasingly efficient due to the discovery of the bulk heterojunction concept [23, 24]. These bulk heterojunctions are achieved

by blending donor and acceptor and they are increasingly based on conjugated polymers. Such blends also exhibit a large interface area and most excitons reach the donor /acceptor interface. Among the organic solar cells derived from blends of conjugated polymers (donor) and fullerenes (acceptor), former constituent absorbs the incident light. The absorption process in the polymer generates an exciton that can either relax back to the ground state or dissociate into an electron and a hole. Nevertheless, organic cells' excitonic diffusion lengths are very small (few nm) and the dissociation process only occurs at the donor/acceptor interface, consequent controlling of a structure of the active layer is very important for an efficient device fabrication. A figure 1.1(a) represents a comprehensive bulk heterojunction organic solar cell. In the given illustration, an active nano-composite layer is sandwiched isolating the electron and hole acceptor bulk electrodes respectively, as depicted by an intimate blend of donor and acceptor organic molecules. The bulk heterojunction organic cell consists of at least four distinct layers on excluding the substrate, which may be glass or some flexible, transparent material as shown in the figure 1.1(a). On the top of the substrate is laid the cathode (through which light enters). Indium tin oxide (ITO) is a popular cathodic material due to its transparency. A layer of the conductive polymer mixture poly (3,4-ethylenedioxythiophene) /poly(styrenesulfonate) (PEDOT–PSS) may be applied between the cathode and the active layer. The PEDOT–PSS layer serves several functions. Not only does it serve as a hole transporter and exciton blocker, but it also smoothens out the ITO surface, seals the active layer from oxygen, and keeps cathode material from diffusing into the active or organic nanocomposite layer, which can lead to unwanted trap sites.

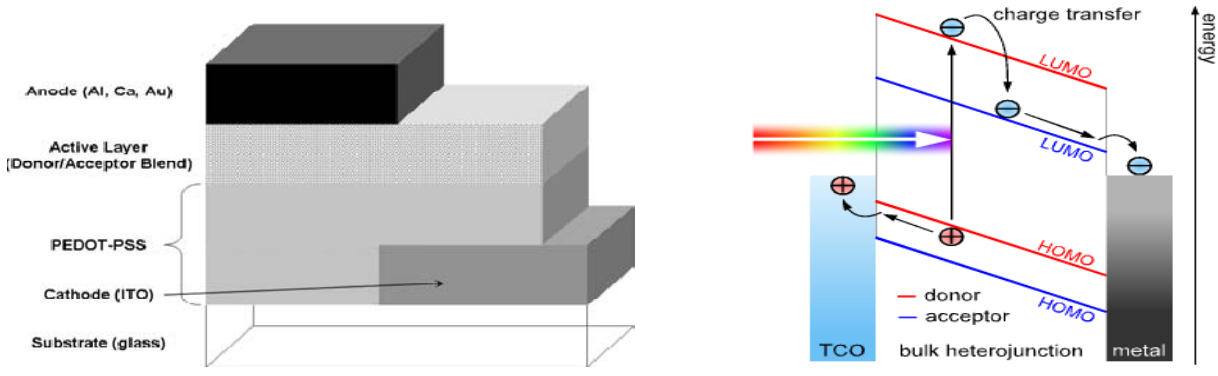

a) b)

Figure 1.1 Diagram (left) of the layered structure of a bulk heterojunction organic solar

cell with active layer comprises of CP/GNR organic composite as donor/accepter blend and flat band diagram (right) of the BHJ device depicting its working principle [25].

The PEDOT–PSS layer is deposited on top of the active layer. The active layer is responsible for light absorption, exciton generation/dissociation, and charge carrier diffusion. The active layer in the heterojunction device consists of two different types of materials, known as a donor and an acceptor; the corresponding materials can be conjugated polymers and carbon nanostructures [26]. On top of the active layer is deposited an anode that is typically made of an aluminum. Alternatively, calcium, silver, or gold can also used. Furthermore, a very thin layer of lithium fluoride (5–10 Å) is usually placed between the active layer and the aluminum anode. The layer of a lithium fluoride that does not seem to react chemically can serve as a protective layer between the metal and organic material. The electrode work functions' levels can be optimized for electron and hole extraction to selectively design a quality diode. An efficiency of the OPV-BHJ device is highly affected by an electronic band gap of the constituents present in active layer apart from the energy level alignment. As depicted in a energy band diagram of the BHJ solar cell (see, figure 1.1(b)), photo induced charge carriers are generated in the electron-donor material, which can be a conjugated polymer (eg. polyaniline) and the electron-acceptor material can be a carbon nanostructure like a graphene nanoribbon. A difference in respective electron affinities in the two nano-components of the active organic layer is a reason for a photoinduced electron transfer. The energetically favorable transition occurs for the electron in the S1-excited state of the conjugated polymer transfers to the much more electronegative carbon nanostructure like GNR or C-60, thus resulting in an effective quenching of the excitonic photoluminescence of the polymer [27]. As a last step, charge carriers are extracted from the device through two selective contacts. A transparent indium thin oxide (ITO) coated glass matching the HOMO level of the conjugated polymer (hole contact) is used on the illumination side, and evaporated thin Lithium Fluoride / Aluminum metal contact matching the LUMO of GNR or PCBM (electron contact) is used on the other side. In the state-of-the-art devices, a thin (100 nm) hole injection layer, a highly doped PEDOT-PSS interfacial layer is used. Due to these stringent requirements of device components, at present the OPV device market is very small, there development is hampered partly also due to non-accomplishment of the present technological needs, namely, lifetime, efficiency and costs [28].

The electron donor's (photon absorber material like PAn or P3HT) optical bandgap is defined by the difference of the band levels of the highest occupied molecular orbital (HOMO) and lowest unoccupied molecular orbital (LUMO). If the photon is absorbed, an exciton is generated. An exciton is a quasi neutral particle and contains a positive and negative charge. An exciton can diffuse at a maximum distance of 20nm in its lifetime [2]. If the exciton does not reach the donor acceptor interface in its lifetime, it will recombine, and the absorbed energy is converted into thermal energy or emitted as a photon and cannot be used for solar power generation. In proviso the exciton reaches the interface and gets dissociated via the electron transferring to the acceptor material. However some energy is lost due to the difference in the LUMO levels of the donor and acceptor material. The as generated charges are driven by drift and diffusion to the electrodes, where they are free to move through the external circuit. For efficient OPVs, however, the as created charge carriers are required to be transported to the corresponding electrodes within their respective lifetimes, which mostly depend on the charge carrier's mobility in the given material. The graphene nanoribbon have a demonstrated width of 1-10 nm and thicknesse of 0.5 nm in addition to excellent electron acceptance and transport characteristics, which allows it to efficiently replace the C-60 in the active layer. It is also to be noted that carrier mobility in graphene is highest until date (>1 $cm^2V^{-1}s^{-1}$) and optical transmittance is as high as 99%. More ever, an aspect ratio (length of ribbon over its width) of nano-ribbon is very high up to >30,000, this it is far more promising material for demonstration of formation of acceptor molecule percolation network within the host PAn chainlike network cage. The development of such a smart nano-composite has far fetching technological applications not to mention again in the improvised light harvesting inside OPVs.

1.2 Polyaniline (PAn)

A lot of attention in the field of polymer science has recently been paid to conjugated polymers, due to their characteristic optical, electrical, and magnetic properties. Most commonly studied classes of conducting polymers are polyacetylene, polythiophene, polypyrrole, polyaniline and their derivatives [29, 30]. Among them, the polyaniline as shown in a figure 1.2 is probably the most widely studied material due to its several unique properties [31, 32]. It exhibits several important technical features of ease of preparation, lightweight, low cost, better electronic-thermal-optical properties, high stability and solubility, good processibility, interesting redox

properties associated with the chain heteroatoms, etc. The PAn is especially suitable for lightweight battery electrodes, hole-injecting electrodes in electroluminescent flexible light-emitting diodes, conductive adhesives electro-magnetic shielding devices, electro-catalysts, anticorrosion coatings, microwave absorption, energy storage and transformation (erasable information storage, non-linear optics) photonic indicators, membranes of precisely controllable morphology, organic actuators, super-capacitors, photovoltaics, transistors, transparent and plastic active and passive devices, and sensors [32–39].

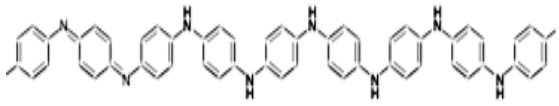

Figure 1.2 Polyaniline (PAn)

The PAn is a semiconducting polymer with wide energy band gap [38]. It belongs to a family of polymers with conjugated backbones [41]. The PAn has three major synthesis forms, which differ from one another by a degree of oxidation 'y' that is a ratio of amine nitrogens over a total number of nitrogen atoms. Fully reduced leucoemeraldine base (LEB) form has the 'y' value of 1 and contains only a C–NH–C amine group in which the carbon 6-rings are phenyl rings with resonantly bonded benzene carbon. Half-oxidized emeraldine base (EB) has the 'y' value of 0.5 as a result of oxidation of half of the nitrogen in the imine form with nitrogen–carbon double bonds in which one-quarter of the carbon 6-rings change character and become quinoids containing carbon double bonds. Fully oxidized pernigraniline base (PNB) has the 'y' value of zero and all imine nitrogen with the carbon 6-rings consist of one-half phenyl and one-half quinoid rings. Each of these forms of PAn is a wide-band gap poor semi-conductor with a band gap of 3.6 eV for LEB and EB and about 1.4 eV for PNB [41–43]. However, the PAn-EB differs substantially from the LEB and the PNB in a sense that its conductivity can be tuned via protonic doping from 10^{-10} up to 10^{2} S/cm and more [44].

Another key property of the conducting polymers is the presence of conjugated double bonds along their backbone, which simply is an alternate single and a double bond arrangement in between the carbon atoms of the chain. The conjugated unit of the chain contains a localized "sigma" (σ) leading to strong chemical bond and an internment electron while the presence of double bond having a less localized "pi" (π) orbital gives weaker bond and a liberated electron

which is free to hop around. However, intrinsically such conjugation in itself is not enough to induced desired electric properties in the polymer.

Previously, it has also been reported by several authors that any wideband gap semiconductor can be made a more useful photo-absorbent by just creating mid band gap states in it, so that its effective absorption lines can be increased for improving the light harvesting for full color range of the solar spectrum. Such useful variants of the otherwise wide energy gap PAn can be prepared through various physical techniques of ion irradiation on a thin PAn film. Here one can irradiate the polymer by a beam of ions and in principle it is possible to place any type of the dopant ions in proximity of aromatic rings of the polymeric backbone chains [45]. It should be noted that such a conjugated-backbone-ion interaction in the PAn brings some local distortion in the chain due to anion π effect and thus the mid energy gap states could start appearing in the electronic structure of the polymer [46]. In a schematic given below (figure 1.3), we have tried to envisage consequences of an electronegative atom (say, chlorine) posed in a proximity of the backbone on the Pan's flat band energy diagram.

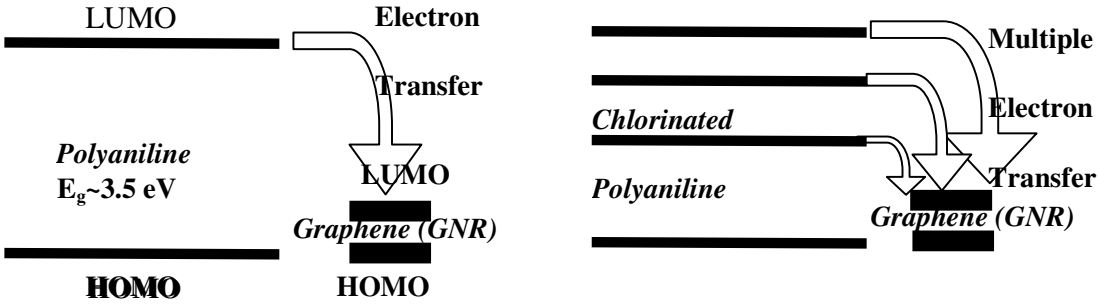

Figure 1.3 Single electron transfer (left schematic) from a fundamental conduction band of the pure polyaniline to the graphene in comparison with a multiple charge transfer (right schematic) from the fundamental gap and various mid gap states in the chlorinated polyaniline. Various sub band states expectably formed by the result of local bond distortion due to proximity of the Cl with the conjugation backbone.

As shown in the figure 1.3 the introduction of sub-band states would not only bring a strong light absorption band in PAn but as well as it will increase the possibility of multiple electron transfer to the graphene nanoribbon, especially in the light of recent reports that percolated nano graphene can accept a number of electrons [1, 7].

1.3 Graphene

Graphene is a two-dimensional (2D) allotrope of carbon that is considered as the mother of all graphitic allotropes because it is the building block for graphite (3D), fullerenes (0D), carbon nanotubes (1D), Nano Ribbons (1D), and Anti dots (0D). Many interesting nanostructures can just be formed either by stacking, wrapping, rolling-up, cutting of graphene sheet or just by applying extreme pressure and temperature on graphene to transform the 2-dimensional sp^2 bonds in to 3-dimensional sp^3 bonds [47]. Graphene in which a monolayer of carbon atoms packed into a dense honeycomb crystal structure is essentially a 2D layer of sp^2 bonded carbon. Carbon atoms of graphene are arranged in a hexagonal structure and has two atoms per unit cell. The carbon-carbon bond length in graphene is approximately 1.42 Å [48]. Graphene is a unique mixture of a semiconductor with zipped density of states and a gapless metal with unusual properties. It has extraordinary electronic excitations (low energy) described in terms of Dirac fermions that move in a curved space. Unlike in the case of metals or common semiconductors, the electrons in graphene obey the Dirac equation rather than the Schrödinger equation [49]. New graphene-physics lead to many exciting and unique properties such as high intrinsic mobility ($2\times10^5 cm^2\ V^{-1}S^{-1}$), and ballisticity up to a few millimeters which give rise to a weak dependence of the mobility on a carrier concentration and temperature, high Young's modulus (~1.0 TPa), high thermal conductivity (~5000 $Wm^{-1}K^{-1}$), immense mechanical strength and flexibility, huge specific surface area (2630 m^2g^{-1}) and largest surface to volume ratio among all the materials on earth, very high optical transmittance of nearly 99%, rapid heterogeneous electron transfer, the graphene also readily exhibits both integer and fractional quantum Hall effect, zero effective mass of its charge carriers and most importantly graphene-nano-devices show spintronic and ballistic transport phenomenon even at room temperature [49–51]. The graphene is widely recognized as a promising material for future electronic devices. Much progress has already accomplished in the fabrication and understanding of graphene's nano-composites, spintronic devices and low on–off current ratio type field-effect transistors (FETs) [52]. The graphene can synthesize by various methods of physical (mechanical exfoliation) and chemical (reduction of graphite oxide and epitaxial growth including chemical vapor deposition) in nature. Recently Javed Mazher et al [2, 53] has reported two very useful methods of the graphene synthesis by using an anodic bonding and an electrochemical intercalation technique.

A structural flexibility of the graphene can be easily explained by using its atomic bonding. A sp^2 hybridization between one *s* orbital and two *p* orbitals lead to a trigonal planar structure in the graphene. Three out of four outer electrons for each carbon atom on a lattice strongly bonded with respective C-neighboring atoms by σ orbitals [52, 54]. A 2 p_z orbital of the fourth electron produces a weaker π bond with a neighboring carbon atom. The σ bonds form the covalent structure with honeycomb geometry. These strong bonds provide a desired mechanical strength, flexibility, and robustness to the graphene's lattice geometry. On the other hand, the π bonds, which describe the intrinsic electronic structure of graphene, are decoupled from the σ bands because of inversion symmetry and they are closer to the Fermi energy in comparison to σ energy positions that separates the occupied and empty states. In a neutral graphene sheet, this is equal to zero energy since valence and conduction bands meet at a point known as charge neutrality point which results in a conical valley shaped bands that touch at two points denoted by their respective momentum vector K and K' in the Brillouin zone, which converts the graphene into a gapless semiconductor. These points are also named as Dirac points. Thus, the graphene is regarded as a many body system in which the electrons are correlated from site to site ensuing a rich collective behavior and strong correlations which are manifested in the form of unique quantum effects and nano-electronic properties [52, 54, 55].

As mentioned above the electrons in graphene obey a linear dispersion relation which can be expressed as, $E = \hbar k v_F = p v_F$, where $p = \hbar k$ is momentum and v_F is Fermi velocity of electrons in the graphene $\sim c/300 = 10^6 ms^{-1}$. Also the $E_{ap} = \sqrt{p^2}$ which implies the effective rest mass is zero [since, the energy of a particle having a rest mass m_0 and moving with a velocity u in a medium is $E = \sqrt{p^2u^2 + m_0^2u^4}$]. Thus, charge carriers in graphene have zero effective mass and simultaneously they move at a very high velocity equivalent to that of speed of light. However, the all-purpose electrons are not actually massless but the effective mass is a parameter that describes how an electron at particular wave vectors responds to applied forces. Since the velocity of electrons confined on the graphene remains constantly high, the parameter (effective mass) vanishes. The Graphene could be semiconductor or a metallic depending on the following factors, (a) Pristine graphene is intrinsically a zero-gap semiconductor because the density of states which can be derived as $D(E) = |E| / 2\pi\hbar^2 v_F$ by using linear dispersion relation

seems to vanish at $E = 0$. But it is observed that the conductivity of the graphene is independent of the fermi energy and the electron concentration as long as variations in effective scattering strength are neglected [55]. Hence the graphene can also be regarded as a metal rather than a zero-gap semiconductor or semi metal. (b) Functionalization process of the graphene rally rounds in creating a gap between the two principal bands (π and π^*) of graphene. That is why, graphene is sometimes considered as a hybrid lying in between a metal and a semiconductor [56]. Crystallographic feature of the graphene can be best described by a triangular lattice with a basis of two atoms per unit cell. Its lattice vectors can be written as

$$a_1 = \frac{a}{2}\left(3, \sqrt{3}\right), \quad a_2 = \frac{a}{2}\left(3, -\sqrt{3}\right) \tag{1.1}$$

where, $a \approx 1.42\,\text{Å}$ is the carbon-carbon distance. Its reciprocal-lattice vectors are given by

$$b_1 = \frac{2\pi}{3a}\left(1, \sqrt{3}\right), \quad b_2 = \frac{2\pi}{3a}\left(1, -\sqrt{3}\right) \tag{1.2}$$

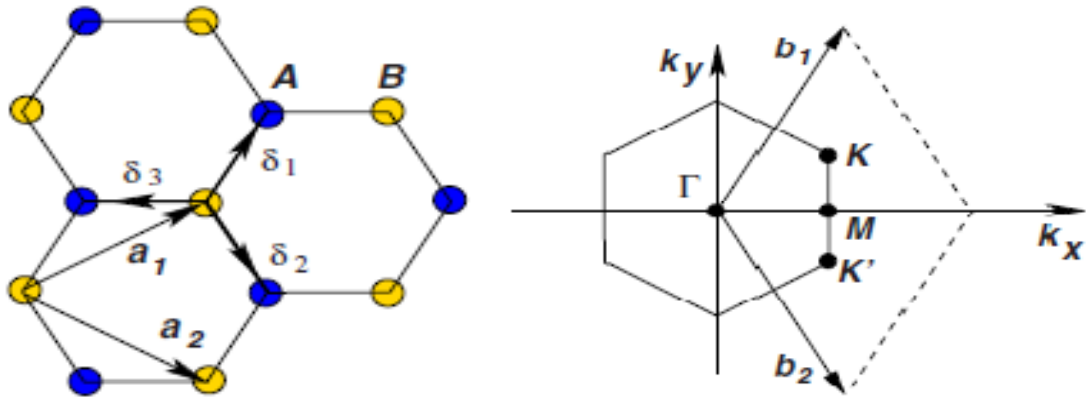

a) b)

Figure 1.4 Honeycomb lattice and its Brillouin Zone (a). Lattice structure of the graphene showing two interpenetrating triangular lattices with a_1 and a_2 as lattice unit vectors, and δ_i, i=1, 2, 3 are nearest-neighbor vectors, (b) corresponding brillouin zone in which the Dirac cones of the linear dispersion curves are located at K and K' points.

An important physics of the graphene is usually spin around the two points K and K′ at the corners of the graphene Brillouin zone (BZ) as shown in a figure 1.4 which are often named as Dirac points. Their positions in momentum space are given by

$$K = \left(\frac{2\pi}{3a}, \frac{2\pi}{3\sqrt{3}a}\right), \quad K' = \left(\frac{2\pi}{3a}, -\frac{2\pi}{3\sqrt{3}a}\right) \tag{1.3}$$

The three nearest-neighbor vectors in real space are given by

$$\delta_1 = \frac{a}{2}\left(1, \sqrt{3}\right) \quad \delta_2 = \frac{a}{2}\left(1, -\sqrt{3}\right) \quad \delta_3 = -a(1,0)$$

while the six second-nearest neighbors are located at $\delta_1' = \pm a_1, \delta_2' = \pm a_2, \delta_3' = \pm(a_2 - a_1)$.

As mentioned above the pristine graphene is a zero band gap semiconductor with its electrons and holes behaving as massless fermions. But the crumpled or functionalized graphene is not and in principle, the fermi energy of functionalized graphene can be easily tuned from valence to conduction band via the external field effect which could be either electrical or chemical potential in nature. Incorporating a local gate can allow the induction of differential charge densities at the different sample regions which could also induced a localized fermi energy variation in which the E_F of one region lies in the valence band (p-type) while in the other region it lies in the conduction band (n-type) [57]. It would be particularly interesting to observe such effects of proximity of organic molecules with graphene, which is usually also the case in nanocomposites of organic polymers blended with graphene.

Graphene Nanoribbons (GNRs)

Graphene nanoribbons (GNRs) are narrow strips of the graphene sheet and obtained by cutting graphene in the form of a quasi-1D wire along a given crystallographic direction [58, 59]. In the graphene nanoribbons, presence of different types of boundary shapes also called as edges are used to modify the electronic structure of the material. The major effects are observed at the Fermi level, displaying unusual magnetic and transport features [60]. For many practical applications, such as in nanoelectronic devices, graphene needs to be patterned into the so-called graphene nanoribbons (GNRs). Typically, graphene is patterned by selectively removing the material by physical/chemical etching techniques [61, 62]. The electronic properties of GNRs are very sensitive to their width and edge geometry [62]. Dependence of edge geometry on the electronic structure of the GNRs has been mainly investigated using theoretical approaches, such as the tight-binding model and density functional theory (DFT) [63]. There are three basic shapes for the graphene edges: zigzag, armchair and hybrid. Nanoribbons with the zigzag edges have less localized edge states at the Fermi energy in comparison to the armchair ribbon.

Types of graphene nanoribbons

a) Zigzag graphene nanoribbon (ZZGNR)

Zigzag nanoribbons have axial symmetry in a form of a single zigzag chain at both side edges along its length as shown in a figure 1.5. In the zigzag graphene nanoribbon, dangling σ-bonds at edges are assumed to be passivated by hydrogen atoms. A width of zigzag nanoribbon is approximately given by $W = (N/4)\ 3a$, where N is the number of atoms in the unit cell. A finite width of the ribbon produces a confinement of the electronic states near the Dirac points [64].

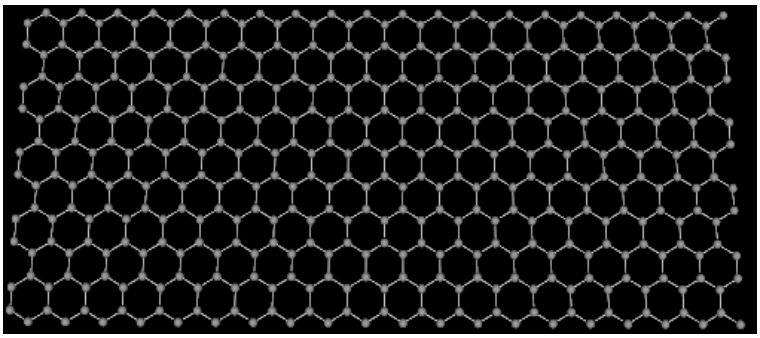

Figure 1.5 Zigzag graphene nanoribbon

Dependence of electronic states on the width of the zigzag nanoribbon may be understood in terms of eigenstates of the Dirac Hamiltonian with appropriate boundary conditions. The crystallographic orientation of the ribbons also determines largely their electronic properties. The Zigzag nanoribbons show a large degeneracy at the Fermi level. The band gap in ZZGNRs can also be controlled by an external electric field. External fields due to gating or attachment of foreign entity can also result in the change of the contributing states in the ZZGNR [65].

b) Armchair graphene nanoribbon (ACGNR)

In an armchair-terminated nanoribbon, the edge consist of a line of dimmers (refer, figure 1.6). The width is related to a number of atoms in the unit cell N through an expression $W = (N/4)\ a$. These ribbons do not have an axial symmetry [64]. The Armchair-terminated graphene systems do not show zero-energy states (the Fermi energy is usually set to zero) [64, 65].

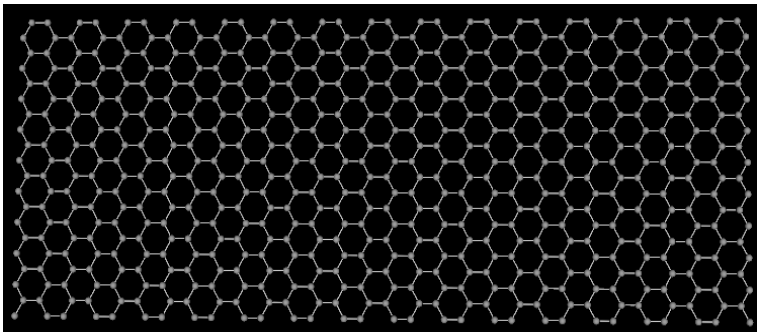

Figure 1.6 Armchair graphene nanoribbon

Electronic properties of the armchair nanoribbon depend strongly on the width, the electronic structure is less affected by ambient, and edge related interactions [66]. A crystallographic orientation of the ribbon determines largely their electronic properties. The electronic structure of the armchair ribbon that is not strongly modified by interactions exceptionally can be modified in the case of metallic ones where a small gap opens [64–67], which is a case of the wider ribbon. Similar to zigzag nanoribbons, electronic properties of the armchair nanoribbon may be understood in terms of eigenstates of the Dirac Hamiltonian with correct boundary conditions [67]. Depending on the value of the number of atoms 'm', the ACGNR can be classified in three categories, namely, m = 3p, 3p + 1 and 3p + 2 (;p is a positive integer) with widely varying electronic properties. The periodic ACGNR with m = 3p + 2 shows some metallic behavior, whereas the other two only show semiconducting behaviors. However, first-principle calculations within the local density approximation (LDA) shows only the semiconducting behavior with a direct band gap at k = 0 for all the three types of ACGNRs and the gap (Δ_a) decreases with increase in the width w_a, and follows a relation of $(\Delta_a) \sim w_a^{-1}$. Nevertheless, in a LDA scheme (local density approximation) also the ACGNR with m = 3p + 2 shows a smaller gap in comparison to other two families. The band gap in ACGNRs is also found to be independent of the ribbon length [68]. However, in the case of m = 3p and 3p + 2 ACGNRs, both HOMO and LUMO show delocalizations along the ribbon length, spanning on the central part. Therefore, the band gap changes significantly with increase in the ribbon length.

c) Chiral and Hybrid graphene nanoribbon (CGNR and HGNR)

Graphene nanoribbons produced by a chemical unzipping of carbon nanotubes are called as chiral ribbons, which are characterized by a low-symmetry orientation of edges in contrast to a

high-symmetry of the zigzag and armchair directions. An unusual presence of edge states are also found in chiral graphene edges [68]. The chirality of the GNR is characterized by a chiral vector (n, m) or, equivalently, by a chiral angle θ [68, 69]. For the high-symmetry zigzag and armchair edges these vectors are (1, 0) and (1, 1), respectively. The edge of (n, m) nanoribbon is a repeating structure composed of n − m zigzag units and m armchair units on providing the n>m. As discussed above the chirality can also be described by the chirality angle θ with a relation, $\theta = \arcsin \sqrt{\frac{3}{4}\left(\frac{m^2}{n^2 + mn + m^2}\right)}$. Zigzag and armchair edges are characterized by $\theta = 0^0$ and $\theta = 30^0$, respectively, while for chiral edges $0^0 < \theta < 30^0$. Thus chiral GNRs are defined by edge translational vectors $(n+1, n)$ and $(n, n+1)\,(n \geq 1)$. These two series cover a whole range of chirality angles θ and converge to $\theta = 0^0$ and 30^0 respectively, with increasing *n*. A hybrid graphene nanoribbon is a mixed nanoribbon which has either of head or tail made up of a one type of GNR and other end is compossed of a different type of ribbon as shown in a figure 1.7. These structures mimic a well-known edge related disorder commonly found in as synthesized GNR nanocomposites.

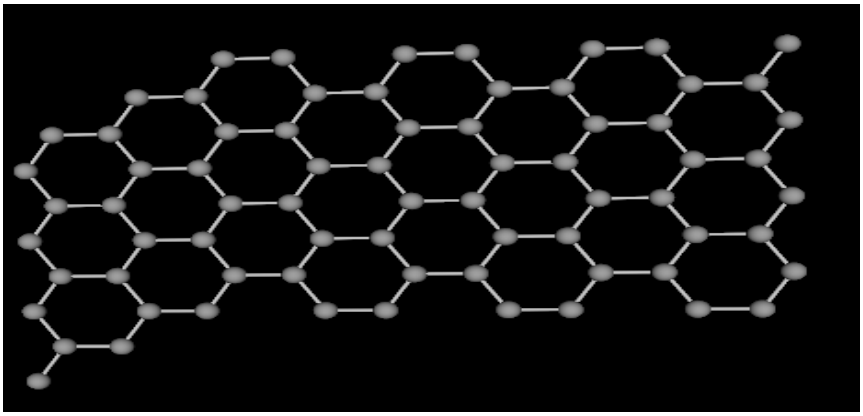

Figure 1.7 Hybrid graphene nanoribbon (HGNR) made up of two ends with different types of ribbons right end is ACGNR and left is ZZGNR.

1.4 Graphene nanoribbon-Polyaniline nanocomposites and their Percolation

To utilize above mentioned novel properties of both the nanocomponent viz GNR and PAn, it is necessary to prepare a nanocomposite in which both the components conserve their individual characters. We know that both the graphene and PAn have conjugated π-electrons, it will be interesting to observe any after effects of this π- π staking on electronic and transport properties of as prepared GNR-PAn nanocomposites from both the fundamental and the application point of view. Nevertheless, for the BHJ solar cells' applications viewpoint, small effect of π- π interactions in between GNR and Pan is better. Such effects are usually discernible in the density of states and the electron transmission spectrum of nanocomposite's two-component system in comparison to that of a pure single component system. Additionally, if percolations happen like the dendrite formation of the individual nano components takes place within the composite material, we can expect some superior transport properties of the bulk heterjunction solar cell. The BHJ solars cell's efficiency will be improved due to these as formed percolative structures because new and efficient individual photo-induced charge transport channels will be created in a form of GNR ribbons and PAn percolating chains, which will scamper via percolation throughout the composite in between ITO and Al electrodes of BHJ cells. Thus, incorporation of graphene sheets into the PAn would definitely enhance the electrical conductivity of the nanocomposite without affecting photo-charge generation rates and efficiencies in the light harvesting material i.e. the PAn. Now it is important to theoretically or experimentally study effects of π- π interactions either on the graphene's electronic transport property or on the electronic structure of the PAn-graphene nanocomposite. In fact, previous studies of UV–vis absorption on them already demonstrated that presence of graphene sheets augment and inflate the fundamental absorption band of the Pan, which is undoubtedly attributed as one of the π conjugation effects [70]. A further step to multifunctional polymer nanocomposites is a development of well-aligned percolating two component nano-systems instead of the dendrite type percolation, as shown in a figure 1.8.

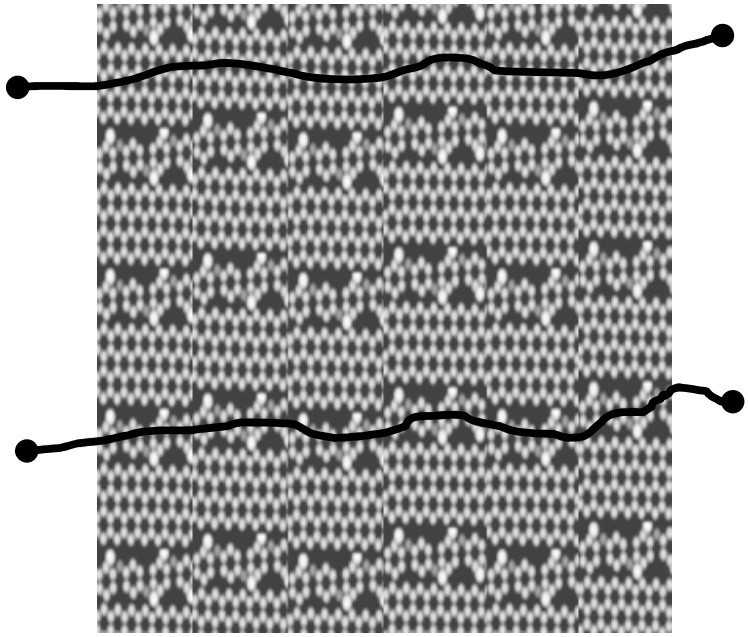

Figure 1.8 Graphene/polyaniline percolating nanocomposite. The top and bottom curved lines are the guide to eye, showing the percolation of graphene nanoribbons and PAn monomeric chains respectively.

1.5 Origin of an equilibrium conductance in nano-devices

It is a common observation among nano-devices that a zero bias conductivity appears at a Fermi energy position. The reason can be ascribed to discrete physical traits of nanodevices when sandwiched in between the charge injection electrodes with continuum physical characters. A small number of conduction states may appear at zero energy levels depending upon a competition that takes place amid following two phenomena.

1. **Fano-effect:** A resonance is thought to be an enhancement of a response of a system to an external excitation at a particular frequency. The Fano resonance (FR) is a universal physical phenomenon, which has historically been discovered, in atomic physics as asymmetric line profiles in spectra of rare gases [71]. The Fano resonance is a consequence of interference amid a localized state and continuum that results in an antisymmetric line shape of the resonance created by the localized state [72]. Very recently, the Fano resonances have been also been observed in condensed matter physics, nano-materials sciences and nano-electronics, both theoretically and experimentally [73]. The said phenomenon can also naturally arises in a coherent electrical transport through a

nanostructured two probe device, in which a central region of the device is comprises of the nanomaterial or a molecule having discrete energy states coupled with continuum states of electrodes. Such a situation creates the Fano resonances near the Fermi level that often strongly enhance an electron transmission through the nano-device [74]. A necessary condition for the Fano resonance is a presence of at least two scattering channels in the form of a discrete level and a broad continuum band in proximity to each other, which is often the case of nano-devices' left and right electrodes and the central scattering region of the nanodevice [74]. The nature of two conduction channels in these mesoscopic systems is highly sensitive to geometries of nano-devices under consideration.

2. **Strong LCR coupling:** On placing nanostructures in between contact electrodes, a sort of charge coupling arises due to formation of strong bonds in between atomic contacts of the central scattering region (C) and the left (L) and the right (R) electrodes, which is covalent in character [75, 76]. Depending upon amount of the charge transfer takes place in between two sides of the atomic contact the strength of coupling increases. Because of the strong coupling some discrete physical traits usually found in the isolated nanostructure like singular energy levels become broadened in the strongly coupled nanostructure. Occasionally, depending upon the amount of charge transfer from electrodes, if these broad energy levels are aligned with chemical potentials of attached electrodes, we usually get small conduction states at the Fermi level of the nanostructure. Hence, the band realignment of the nanostructure is responsible for low energy charge carrier conduction in the 2 probe devices [77].

Therefore, either a switching or a rectification in the nanodevice arises due to the Fano effects or the strong coupling induced singularities. One of the ways to explore their signatures is study of density of states and non-equilibrium electron-transmission spectra of the nano device having a quantum confined central region. Usually, in nanoelectronics two probe devices, the rectification does not usually happen by the schottky barrier effect because the nature of both contact electrodes and the sample material in consideration are purely mesoscopic in nature. Moreover various atomistic ab-initio modeling studies show that bulk contacts are absent in the nanodevice instead only pure atomic scale contacts are formed [73, 74]. This implies that the I–V characteristics and the rectification behavior (if any) in the device mainly depends upon (a) Electrode materials and their dimensionality, whether they are one dimensional or two

dimensional, (b) Singularities present in the density of electronic states of the nanostructure located at the central region (sample to be tested) of the device, (c) Interfaces and a contact geometry of the electrode and the central region and (d) A coupling strength between the two ends of the central region with electrodes [78]. Often the strong coupling results in sharp and intense DOS peaks near the Fermi level and the weak coupling gives a broader DOS resonant states. This effect is also earlier reported in the density of states and the transmission energy spectra along with I-V measurements [73, 74], where a ohmic contact is observed instead of a rectification at the nanometallic/nano- semiconductor atomic interface. Indeed, Fano line shapes are also observed in a differential electrical conductance (dI/dV) plot with bias voltage during a tunneling course using a scanning tunneling microscope and through an impurity atom on a metallic surface [71, 73, 74]. In contrast, the Fano antiresonance dips are reported in the density of states and the transmission spectrum of nano-devices at the Fermi level when an injection of states from electrodes to the central region is destructive in its interference with states present in the central region, which is manifested in the rectifying behavior of the nanodevices [74, 78].

1.6 Singularity in quantum confinement of nanostructures

Low dimensional systems with electron confinement such as 2-D quantum wells, 1-D quantum wires or 0-D quantum dots exhibit interesting new physical properties of discrete in nature due to their unique electronic energy band structure, which often results in singularities of an electronic state density in respect to an energy. This is reasonably well explained by various 1D to 3D free motion confinement models [76]. The reduced dimensionality of an electron gas has a profound influence on the nanowire or the atomic chain's density of states (DOS). A recent interest in quantum wires arises partially from an inverse square-root relation of the DOS with its electronic energy. It is interesting to note that the coulomb correlation effects in 1D systems further reduces interband transitions near the band gap [79, 80] at least partially counteracting effects of singularities in the density of states. The discrete nature of electronic states in quantum structures and dynamics of a relaxation of carriers between these discrete states are two of the areas of interest in the most recent investigations in the field of nanoelectronics. Within the realm of nanoscience and nanotechnology, nanostructures like nanowires, graphene nano-ribbons, etc play a special role because of their one dimensionality.

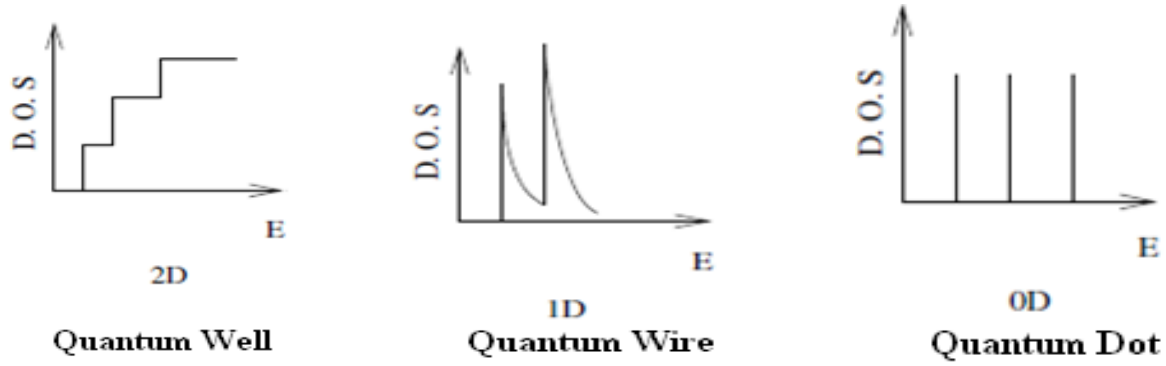

Figure 1.9 Density of states of 2, 1, 0 dimension nanomaterials.

When the nanomaterial's dimensions such as GNR's width or nanowire's diameter is made smaller, the singularity in the electronic density of states developed at certain specific energy. The singularities exhibit size dependent spectral positions in DOS spectra sometimes often referred as van Hove singularities, where the electronic density of states become very large (see, figure 1.9), resembling more closely a case of molecules and atoms and appearing to be very different from a case of crystalline solids or even two dimensional systems [81, 82]. In the limit of small diameter nanostructure with large aspect ratios such as nanowires or nanoribbons, different positions and shapes of these singular densities of states have dramatic effects on the nano-electronic properties of the device.

CHAPTER TWO

2. Objectives

2.1 General objectives

The general objectives of this thesis work are

- To study electronic and charge transport properties of the novel graphene nanoribbon and polyaniline nanocomposites.

2.2 Specific objectives

The specific objects are

- Study of suitability of the Graphene nanoribbon-Polyaniline (GNR-PAn) nanocomposite material with its novel photovoltaic properties for solar energy applications.
- Ab initio DFT, LDA, NEGF based simulation in different GNR-PAn samples in novel configurations are performed to study the electronic and transport properties of this nano-organic semiconductor.
- Development of an integrated and a generalize approach for modeling the percolating nanocomposite by using first principle simulation techniques.

CHAPTER THREE

3. Methodologies and Simulations

3.1 Modern Theoretical Methods

3.1.1 Ab initio Techniques

Ab-initio techniques or first principle approaches are based on using a fundamental Hamiltonian of a given physical system for deriving its basic electronic and physio-chemical properties [83]. An exact solution of a resulting many-body (N-electron) Schrödinger equation is almost impossible and hence some approximations are deployed in such calculations. The approximations are purely technical in nature. A determinantal form of the many-body wavefunction is used in a Hartree-Fock approximation and a representation of its single-particle ingredients is achieved from a finite basis sets. All such technical simplifications help in reducing the ab-initio calculation time. Nevertheless, the ab-initio simulation is characterized by the fact that its approximations do not introduce adjustable physical parameters. The universal Hamiltonian of any coupled electron-nucleus system is,

$$\hat{H} = \hat{T}_n + \hat{V}_{n-n} + \hat{H}_e \quad \left(+\hat{V}_{n-field}\right) \tag{3.1}$$

$$\hat{H}_e = \hat{T}_e + \hat{V}_{n-e} + \hat{V}_{e-e} \quad \left(+\hat{V}_{e-field}\right) \tag{3.2}$$

In Eq. (3.1) $\hat{T}_n$ represents the kinetic energy of the K nuclei of the system,

$$\hat{T}_n = \sum_{\alpha=1}^{K} \frac{\left(-i\hbar\nabla_{R\alpha}\right)^2}{2M_\alpha} \tag{3.3}$$

where, R_α denotes the Cartesian coordinates of nucleus α with mass M_α and $\nabla_{R\alpha} = \partial/\partial R_\alpha$. A potential $\hat{V}_{n-n}$ represents the repulsion amongst nuclei.

$$\hat{V}_{n-n} = \sum_{\alpha,\beta=1;\alpha<\beta}^{K} \frac{Z_\alpha Z_\beta e^2}{\left|R_\alpha - R_\beta\right|} \tag{3.4}$$

As the theoretical research problem undertaken for present thesis-work is purely electronic in nature and the $\hat{V}_{n-n}$ just amounts to an additive constant. The third component of $\hat{H}$ is the electronic Hamiltonian $\hat{H}_e$, which is decomposed into the kinetic energy of the *N* electrons,

$$\hat{T}_e = \sum_{i=1}^{N} \frac{(-i\hbar\nabla_i)^2}{2m} \tag{3.5}$$

$(\nabla_i \equiv \nabla_{r_i}$, with r_i denoting the position of electron $i)$, the interaction between electrons and nuclei (with charges $Z_\alpha e$, $e = |e|$),

$$\hat{V}_{n-e} = -\sum_{\alpha=1}^{K}\sum_{i=1}^{N} \frac{Z_\alpha e^2}{|R_\alpha - r_i|}, \tag{3.6}$$

and the interaction among the electrons,

$$\hat{V}_{e-e} = \sum_{i,j=1;i<j}^{N} \frac{e^2}{|r_i - r_j|} \tag{3.7}$$

As stated earlier, the Schrödinger equation for any system of many body cannot be easily solved analytically or numerically [84] and due to the fact that our system is purely electronic and hence we can consider the Born Oppenheimer approximation (BOA). The BOA takes into account a fact that due to a big difference between an electronic mass and nuclei mass, the electron motion far supersedes any displacement of the nuclei, therefore, we can consider the nuclei fixed in its position, and solve the equation of motion for the electron in electrostatic potential arising from the particular arrangement of the nuclei. In most basic terms, the BOA allows the wavefunction of a solid to be adiabatically broken into its electronic and nuclear (variational, rotational) components.

$$\psi_{total} = \psi_{electron} \text{x } \psi_{nuclear} \tag{3.8}$$

In the first step of BOA, the electronic Schrödinger equation is solved, yielding the wavefunction $\psi_{electron}$ depending on the electrons only. Meanwhile classically defined nuclei are fixed in a certain configuration and in the equilibrium. A set of electronic energies thus computed becomes a function of the nuclear coordinates. Further, this function serves as a potential in a Schrödinger equation containing only the nuclei. The success of BOA is due to the high ratio between nuclear and electronic masses that is followed by the inertia of electrons being considered to be negligible in comparison to the atom to which they are bound.

The earliest successful quantum mechanical formulation is the Hartree-Fock (HF) method**,** used to calculate a ground-state wave-function and an energy of the system of many-bodies which is appreciated by the fermionic mean field theory [83, 84]. The method assumes

that the exact, N body wave function of the system can be approximated by a single Slater determinant of N orbitals. By invoking the variational principle, one can derive a set of N-coupled equations for N orbital solution of these equations that yield the Hatree-Fock wave function and the energy of the system, which are the approximations of the exact ones. Nevertheless, the real physical properties are difficult to obtain from pseudo symmetric methods like HF self-consistent methods, partially owing to the fermionic antisymmetricity induced by the Pauli's exclusion and other exchange correlations. All this leads to larger inferences in energy gaps of electronic materials and an illusory non-matallicity.

3.1.2 The Density Functional Theory (DFT)

Use of the electron density instead of the wave-function is introduced by Thomas and Fermi [84, 85] as early as 1927 to effectively describe the electronic structure in atomic and molecular systems. However, this rudimentary model only takes into account the kinetic energies of involved constituents. In a way, the Thomas-Fermi and Hartree-Fock-Slater methods can be regarded as ancestors of modern DFT. The chief building blocks of these traditional methods are single-electron orbitals, and many-electron wave functions constructed from them. Thus the chief elements of the modern DFT are the electron density $n(r)$ and fictitious single-particle orbitals.

The density functional theory is phenomenally successful in finding solutions to the fundamental Schrödinger equation that describes the quantum behavior of atoms and molecules. Gradually this ab-initio DFT approach has spurt out from clutches of few physicists to the wide spread scientific community which is using the quantum mechanical theory to as a tool in solving problems of chemistry, physics, materials science, chemical engineering, geology, and other disciplines. Conceptually the DFT describes the ground state energy of a system of interacting electrons in an external potential as a functional of the ground state electronic density [84, 85] and the given material's electronic ground state structure is given in terms of the electronic density distribution $n(r)$. In the Kohn-Sham DFT formulation [85] the ground state density can be written in terms of the single-particle orbitals. The single particle orbital ϕ is obtained a priori by using atomic pseudopotentials [86]. Ideally, a pseudopotential is developed by considering an isolated atom of one element, but the resulting pseudopotential can then be used reliably for calculations that place this atom in any chemical environment without further adjustment of the

pseudopotential. This desirable property is referred to as the transferability of the pseudopotential. Current DFT codes typically provide a library of norm conserving pseudopotentials that includes an entry for each (or at least most) elements in the periodic table.

The entire field of density functional theory rests on two fundamental mathematical theorems proved by Kohn and Hohenberg and a derivation of the set of equations by Kohn and Sham [87]. The former theorem of Hohenberg and Kohn proves that the ground-state energy from Schrödinger's equation is a unique functional of the electron density and states that there exists a one-to-one mapping $E[n(r)]$ between the ground-state wave function and the ground-state electron density $n(r)$. The second theorem essentially describes a nature of this density functional along with its properties. Accordingly, the electron density that minimizes the energy of the overall functional is the true electron density corresponding to the full solution of the Schrödinger equation. A useful way to write down the functional is described by the later Hohenberg - Kohn theorem in terms of a single-electron wave function, $\psi_i(r)$. These functions collectively define the density $n(r)=\sum f_i|\psi_i(r)|$. The energy functional can be written as

$$E[\{\psi_i\}]=E_{known}[\{\psi_i\}]+E_{XC}[\{\psi_i\}] \tag{3.9}$$

where, the functional splitted into two parts, $E_{known}[\{\psi_i\}]$ and everything else, E_{XC}. The "known" terms include four contributions:

$$E_{known}[\{\psi_i\}]=\frac{h^2}{m}\sum_i\int\psi_i^*\nabla^2\psi_i d^3r+\int V(r)n(r)d^3r+\frac{e^2}{2}\int\int\frac{n(r)n(r')}{|r-r'|}d^3rd^3r'+E_{ion} \tag{3.10}$$

The terms on the right are, in order, the electron kinetic energies, the Coulomb interactions between the electrons and the nuclei, the Coulomb interactions between pairs of electrons, and the Coulomb interactions between pairs of nuclei respectively. The other term $E_{XC}[\{\psi_i\}]$, is the exchange–correlation functional defined to include all the quantum mechanical effects that are not included in the "known" terms. This undefined exchange– correlation energy functional can be expressed by Kohn and Sham equations, which have the form

$$\left[\frac{\hbar^2}{2m}\nabla^2+V(r)+V_H(r)+V_{XC}(r)\right]\psi_i(r)=\varepsilon_i\psi_i(r) \tag{3.11}$$

These equations are superficially similar to a more complete description of the Schrödinger equation which is

$$\left[\frac{\hbar^2}{2m}\sum_{i=1}^{N}\nabla_i^2+\sum_{i=1}^{N}V(r_i)+\sum_{i=1}^{N}\sum_{j<i}U(r_i,r_j)\right]\psi=E\psi \qquad (3.12)$$

The main difference is that the Kohn–Sham equations are missing the summations that appear inside the full Schrödinger equation (Eq. 3.12). This is because the solutions of the Kohn–Sham equations are single-electron wave functions. On the left-hand side of the Kohn–Sham equations there are three potentials, V, V_H, and V_{XC}. The first of these also appeared in the full Schrödinger equation (Eq. 3.12) and in the "known" part of the total energy functional given above (Eq. 3.11). This potential defines the interaction between an electron and the collection of atomic nuclei. The second is called the Hartree potential and is defined by

$$V_H(r)=e^2\int\frac{n(r')}{|r-r'|}d^3r' \qquad (3.13)$$

This potential describes the Coulomb repulsion between the electron being considered in one of the Kohn–Sham equations and the total electron density defined by all electrons in the problem. The Hartree potential includes a so called self-interaction contribution because the electron we are describing in the Kohn–Sham equation is also a part of the total electron density, so a part of V_H involves a Coulomb interaction between the electron and itself. The self interaction is unphysical, and the correction for it is one of several effects that are lumped together into the final potential in the Kohn–Sham equations, V_{XC}, which defines exchange and correlation contributions to the single electron equations. V_{XC} can formally be defined as a "functional derivative" of the exchange–correlation energy:

$$V_{XC}(r)=\frac{\delta E_{XC}(r)}{\delta n(r)} \qquad (3.14)$$

The strict mathematical definition of a functional derivative is slightly more subtle than the more familiar definition of a function's derivative, but conceptually we can think of this just as a regular derivative. The functional derivative is written using δ rather than d to emphasize that it is not quite identical to a normal derivative. To solve the Kohn– Sham equations, we need to define the Hartree potential, and we need to know the electron density. But to find the electron density, we must know the single-electron wave functions, and to know these wave functions we must solve the Kohn–Sham equations. To break this circle, the problem is usually treated in an

iterative way as outlined in the following algorithm also called as the Hohenberg-Kohn-Sham scheme.

1. Define an initial, trial electron density, $n(r)$
2. Solve the Kohn-Sham equations defined using the trial electron density to find the single-particle wave functions, $\psi_i(r)$
3. Calculate the electron density defined by the Kohn-Sham single-particle wave functions from step 2, $n_{KS}(r) = 2\sum_i \psi_i^*(r)\psi_i(r)$
4. Compare the calculated electron density, $n_{KS}(r)$, with the electron density used in solving the Kohn-Sham equations, $n(r)$. If the two densities are the same, then this is the ground-state electron density, and it can be used to compute the total energy. If the two densities are different, then the trial electron density must be updated in some way. Once this is done, the process begins again from step 2.

3.1.3 Approximations for Exchange – Correlation Functional

As discussed above the Hohenberg – Kohn – Sham scheme can be accurately implemented only when explicit form of the exchange-correlation functional is known, but in real materials it is simply anonymous. Hence we use a necessary approximation for exchange-correlation potential. Fortunately, there is one case where this functional can be derived exactly: the uniform electron gas in which the electron density is constant at all points in space; that is $n(r) =$ constant and we set the exchange-correlation potential at each position to be the known exchange-correlation potential from the uniform electron gas at the electron density observed at that position:

$$V_{XC}(r) = V_{XC}^{electronga\ s}[n(r)] \qquad (3.15)$$

This approximation uses only the local density to define the approximate exchange–correlation functional, so it is called the local density approximation (LDA). LDA is the oldest and simplest way of solving the variational equations [88]. The LDA gives us a way to completely define the Kohn– Sham equations, but it is crucial to remember that the results from these equations do not exactly solve the true Schrödinger equation because we are not using the true exchange–correlation functional. The exchange energy is the contribution to the energy and results from the Pauli principle that no two electrons of the same spin energy can reside in one state. The

correlation energy is the contribution to the energy from the Coulomb repulsion that an electron experiences from all other electrons. E_{XC} thus depends on the electronic density. As the exact solution of the n-body problem is not known, therefore one cannot have any idea a priori about the behavior of $E_{XC}[n]$. This assumes that the exchange - correlation potential for an electron is equal to the exchange-correlation potential of an electron in a uniform gas of interacting electrons. Nevertheless, the type and nature of approximations are often the material system and the problem specific. Best-known class of the functional after the LDA uses information about the local electron density and the local gradient in the electron density. This approach defines a generalized gradient approximation (GGA). The GGA includes more physical information than the LDA and so it must be more accurate. In addition, there are many alternative ways to include the information from the gradient of the electron density in the GGA functional.

In summary the Ab-initio DFT methods have the advantage that they have to converge and not necessarily in monotonic fashion to the exact answer in the given basis set and the correlation limit. Hence, the ab initio DFT method can essentially be summarized in following five elements: (1) all calculations are done in a basis set (usually Gaussian Functions), (2) a rigorous, orbital dependent, energy functional for the exchange and the correlation is taken from wave-function theory, (3) there is a convergence to the right answer in the basis set and correlation limit, (4) the Kohn-Sham determinant as calculated in the method provides a correct and correlated density consistent with a corresponding functional, as required by the DFT, (5) the potentials are multiplicative and as required by the DFT, but the functionals are nonlocal [88].

3.1.4 The Non-Equilibrium Green's Function (NEGF)

Despite its mathematical complexity, the NEGF method for calculation of quantum transport has gained great popularity in recent years, mostly because of the versatility and numerical stability of the method, in contrast to wave function or transfer matrix approaches. The open boundary conditions can be elegantly included by exactly mapping the contacting leads into a finite and small part of the system [89]; furthermore, the Green's function approach can be generalized to many-body quantum theory, allowing the inclusion of electron–phonon as well as electron–electron interactions within a unified and systematic formalism [90]. Non equilibrium Green's function methods are usually employed as a basic theory to build quantitative models for

studying the transport properties in nanoscale conductors under voltage difference and for quantum device simulation [91]. It is used for calculating current, effective potential and charge densities in nanoscale (both molecular and semiconductor) conductors under bias. In order for any program to simulate a quantum device, a self-consistent solution of a transport Eq. 3.16 must be performed. The calculations of the electron density and the effective potential are iterated till they converge to a self-consistent value. The I–V characteristics have been calculated with the Landauer formula [92]

$$I = \frac{2e^2}{h}\int_{-\infty}^{\infty} T(E)[f_l(E) - f_r(E)]dE \qquad (3.16)$$

where e is the electron charge, h is Plank's constant, and $f_l(E), f_r(E)$ represent the Fermi distribution functions at the left and right electrodes, respectively. $T(E)$ stands for the transmission coefficient as a function of the electron energy E .

3.2 Methodologies for Atomistic Simulation

3.2.1 SIESTA

SIESTA (Spanish Initiative for Electronic Simulations with Thousands of Atoms) is both a method and its computer program implementation, to perform electronic structure calculations and ab initio molecular dynamics simulation of molecules and solids. Its main characteristics are

- It uses the standard Kohn-Sham self consistent density functional method in the local density approximation (LDA) or general gradient approximation (GGA).
- It uses norm-conserving pseudopotentials in their fully nonlocal form.
- It uses atomic orbital as a basis set allowing unlimited multiple-zeta and angular momenta polarization and off-site orbitals.
- Projects the electron wave functions and density onto a real-space grid in order to calculate the Hartree and exchange-correlation potentials.
- Simulations with several hundred atoms are feasible with modest workstations.

It routinely provides the total and partial energy, atomic forces, stress Tensor, electric dipole moment, band structure, electron density and atomic, orbital and bond populations (Mulliken).

TRANSIESTA provides the ability to model the open boundary systems where ballistic electron transport is taking place. Using TRANSIESTA one can compute electronic transport properties, such as the zero bias conductances and the I–V characteristic of a nanoscale system in contact with two electrodes at different electrochemical potentials. The method is based on using non equilibrium Green's function (NEGF), that are constructed using the density functional theory Hamiltonian obtained from a given electron density. A new density is computed using the NEGF formalism, which closes the DFT-NEGF self consistent cycle. The present Siesta release [93] includes the possibility of performing calculations of nano-electronic transport properties in combination of TranSiesta method which deploys a finite material structure sandwiched in between two semi-infinite metallic leads and gives a solution of the electronic structure of such an open system device. A finite bias can be applied between both leads to drive a finite current. In brief, the calculations using TranSiesta involve first the device's electronic density elucidation from the DFT Hamiltonian using Green's functions techniques followed by I–V calculations.

3.2.2 The Python language

Python is deployed in SIESTA/ TranSIESTA source codes since 2004 and since then a significant amount of related codes have been written in Python. Python is an easy to learn, powerful programming language. It has efficient high-level data structures and a simple but an effective approach to object-oriented programming. Programs written in Python are typically equivalent to C++, or Java programs [94, 95]. It is easy to combine Python with compiled languages, like C++, which are widely used languages for scientific computations. The important features of Python are as follows,

- A simple and a minimalistic language. It allows us to concentrate on the solution to the problem rather than the language itself.
- A free and an open source. It is a FLOSS (Free/Libre' and Open Source Software) based on the concept of a community which shares knowledge and is constantly improved by the user community.
- A high level language.
- Portablility. It can be ported to many platforms. All our python programs can work on any of these platforms without requiring any changes at all if we are careful enough to avoid any system-dependent features.

- Interpretability. Python does not need a compilation to binary.
- Object oriented. Python supports object oriented programming (OOP). The program is built around objects which combine data and functionality.
- Extendable libraries. The python standard library is huge indeed and it also supports external libraries of ATK, etc [96].

3.2.3 The Atomistix software package

Atomistix provides two different interfaces for performing electronic transport calculations: Virtual Nanolab (VNL), which is a graphical user interface (GUI) and Atomistix Toolkit, which is a file-based or command line interface. The atomistix toolkit (ATK) gives more control and flexibility through the scripting. The strength of ATK and VNL lies in their flexibility to describe systems of different symmetries.

3.2.3.1 The Atomistix Toolkit (ATK)

ATOMISTIX TOOLKIT is a library of atomic scale modeling techniques that can be used to calculate a wide range of properties of nanoscale systems. New methods are constantly being added to the toolkit, and for each new release ATK will be able to calculate more properties using a wider range of different modeling techniques. The most unique feature is the ability to calculate the electrical properties of nanoscale devices, which consist of a scattering region coupled to two macroscopic bulk systems or electrodes. ATK provides methods for describing three different system types; molecular, bulk, and two-probe systems. A two-probe system consists of a nanoscale region coupled to two macroscopic bulk systems, or electrodes. The nanoscale region can be a molecule, nanotube, cluster of atoms, a piece of a semiconductor or an interface between the electrodes. The description of the electronic structure in ATK is based on density functional theory [97] and an important ingredient in the calculations is the approximation used for the exchange–correlation functionals.

ATK is a first-principles electronic structure program capable of modeling electrical properties of nanoscale systems coupled to semi-infinite electrodes. In short, the key features in ATK are calculations of electrical properties of nanoscale devices, access to advanced DFT algorithms, support of molecular systems, bulk and periodic systems, and two-probe systems and python-based NanoLanguage scripting environment.

3.2.3.2 The Virtual NanoLab (VNL)

Virtual NanoLab gives us access to a powerful set of modeling tools for investigating nanoscale structures through a user friendly graphical interface. The VNL software uses advanced software architecture and numerical methods to find solutions of the fundamental quantum mechanical equations describing the electronic properties of nanoscale objects, such as molecules, bulk and two-probe systems by use of the techniques Density Functional Theory and Non-equilibrium Green's Functions**.** Based on the these techniques, VNL can simulate the detailed electronic structure and transport properties of molecules, crystals, nanotubes, and two-probe devices. The way we work with VNL is in many aspects similar to what we would do in an actual experiment:

1. First we set up our system using either of the Molecular Builder, the Crystal Cupboard, or the Atomic Manipulator tools.
2. After setting up our system, we specify the details of the DFT method that should be applied to our system. We do this using either the Method Editor or the NanoLanguage Scripter tool.
3. Once the DFT method has been defined, we select the physical properties that should be extracted from the calculation. We do this by using the NanoLanguage Scripter tool.
4. The calculation is then performed by submitting the job to the Job Manager tool or executing it from the command line.
5. Finally, we analyze and inspect the obtained data by using the Nanoscope and the Result browser tools.

In short, VNL is designed to bridge experimental and computational approaches by offering a spectrum of useful tools for performing virtual experiments. The NanoLanguage scripts that are generated with VNL are performed with the Atomistix Toolkit (ATK) calculation engine. Since VNL is designed with ease-of-use in mind, we do not have to be an expert in quantum chemistry and electronic structure calculations to use it. Instead, we can focus on the physical properties of the systems under investigation, and let the program handle the details of the numerical models. The numerical methods used in VNL are primarily based on first principles (ab initio) and do not, in principle, require any input parameters regarding the quantum-mechanical description of the atomic systems. Nevertheless, as is the case in most numerical simulations, a number of accuracy parameters must be specified to define the density functional theory and Non-equilibrium green’s functions methods. Virtual NanoLab (VNL) offers a rich set of powerful

tools for investigating and analyzing the properties of nanostructures by simulating measurements through numerical calculations. It gives scientists, engineers, and researchers access to powerful atomic scale modeling tools by means of an easy-to-use graphical interface. VNL provides convenient programs to design and build several types of nanostructures, setup scripts for performing calculations and inspect, analyze, and visualize our results. Numerical calculations in VNL is processed by the Atomistix Toolkit, which combines advanced numerical methods, such as density-functional theory and non-equilibrium Green's functions**,** to describe the detailed electronic structure of nanoscale devices. The most unique capability of VNL is the ability to investigate the electronic transport properties of nanoscale devices. Advanced numerical algorithms enable the application of a bias voltage across the structure, as well as the calculation and analysis of current-voltage characteristics of so-called two-probe systems.

All tools in VNL can also interpret Python code. This can be used to define a more complex geometry as a set of logical or repetitive operations in a script, which then directly can be used as input to the next step in the work flow. VNL is also extensible through user-defined plug-in components that can build special structures and perform specific analysis and plotting. The Toolbar icons give us quick access to tools used for creating and modifying molecule, bulk, and two-probe systems, setting up density functional theory calculations and defining the physical properties that should be extracted from the calculations and executing calculations, as well as inspecting and analyzing results.

Table 3.1 Summary of various tools accessible in the VNL

Tool	Icon	Description
Molecular Builder		Build and construct our own molecules ready to be used in other VNL tools
Atomic Manipulator		Set up two-probe systems and make modifications to magnetic tunnel junctions.
NanoLanguage Scripter		Create complete calculation set-ups and store these as Nano-Language script.
Method Editor		Predefine DFT and NEGF parameters for reuse in the Nano- Language Scripter when generating NanoLanguage scripts.
Script Editor		Manually edit and extend NanoLanguagescripts constructed by the different set of VNL tools.
Job Manager		Execute scripts using the ATK computation engine.
Nanoscope		Visualize atomic geometries and calculated properties in 3D.
Result Browser		Browse the contents of VNL files including all stored samples and results within them.

3.2.4 Samples and simulation methods for GNRs, PAn and GNR-PAn devices

We have prepared a set of seven different two probe devices (D1 to D7), which are electrically connected through metallic Lithium atomic-chain electrodes of high electrical transmitivity even at higher voltages. The central region of the as prepared nano electronic device is packed with various samples of pristine chlorinated PAn to ZZ/AC/H GNRs and the GNR-PAn nanocomposites respectively in various conformations. Our nanocomposite conformations are

mainly comprised of parallel plane and in-plane conformations. The parallel plane is the situation when both the PAn chain and the nano-ribbon are in different planes but in proximity with each other in the direction of transmission device while the later conformation lies in the same plane.

Table: 3.2 Details of various devices from D1 to D7

Device No	**Sample placed in the central region**	**Central region width**	**Remark**
D1	Chlorinated PAn	21.5 Å	Organic molecule
D2	ZZ-GNR of width 8 repetition 8	21.6 Å	GNR
D3	AC-GNR of width 8 repetition 5	21.9 Å	GNR
D4	H-GNR width 8 repetition 6	21.5 Å	GNR
D5	ZZ-GNR/PAn nanocomposite	21.5 Å	Parallel plane conformation
D5	AC-GNR/PAn nanocomposite	21.7 Å	In plane conformation
D7	H-GNR/PAn nanocomposite	21.5 Å	Parallel plane conformation

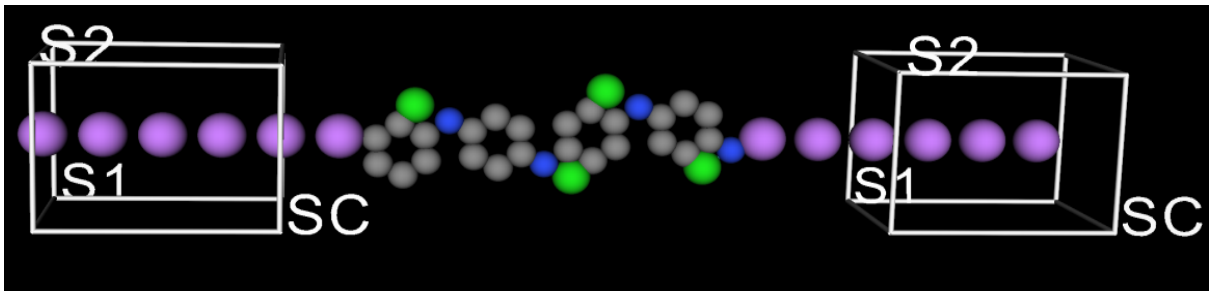

Figure 3.1 Two probe device (D1) in which a central region constitutes of a modeled structure of the polyaniline (PAn) chain and the proximate chlorine (Cl) atoms. In the central region, C-C, N-C and N=C bond lengths are set to be 1.42 Å, 1.47 Å and 1.29 Å respectively while the N:Cl^- distance is 1.75 Å. (Blue sphere = N, Gray = C, Green = Cl, Magenta = Li). The Li-Li inter-atomic distance of source-drain electrodes is 2.9 Å. The left and right electrodes are very high conductivity Li-atomic chains that are metallic in character and provided with up to three electron transmission channels.

A figure 3.1 shows the first device with a central region of the polyaniline in relax-pose atomic positions (in Å) at tolerance of less than 0.001 eV. The PAn is modeled in the chlorinated form to increase energy mid-band gaps states for achieving improved light harvesting and photo induced charge transfers as discussed before in the introductory section. The light harvesting in the PAn chain is expected to increase with its proximity to highly electronegative chlorine atom.

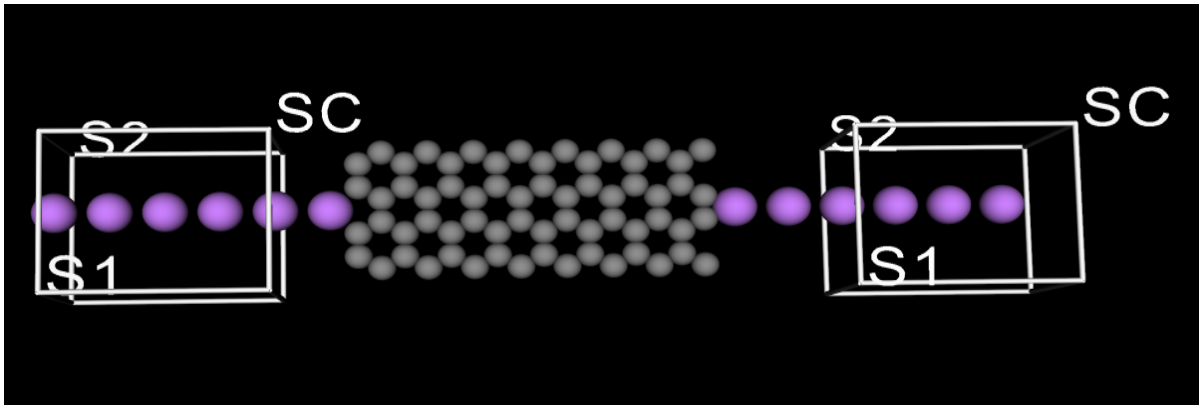

Figure 3.2 (a) Two probe device (D2) in which the central region constitutes of a modeled structure of ZZ-GNR having width of 8 C-atom layers and along length there is a repetition of 8 C-atom unit cells.

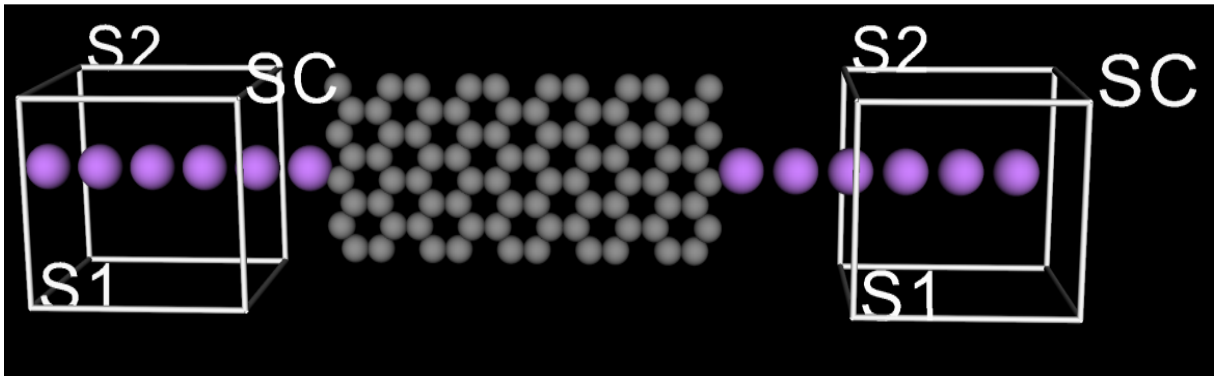

Figure 3.2 (b) Two probe device (D3) in which the central region constitutes of a modeled structure of AC-GNR having width of 8 C-atom layers and along length there is a repetition of 5 C-atom unit cells.

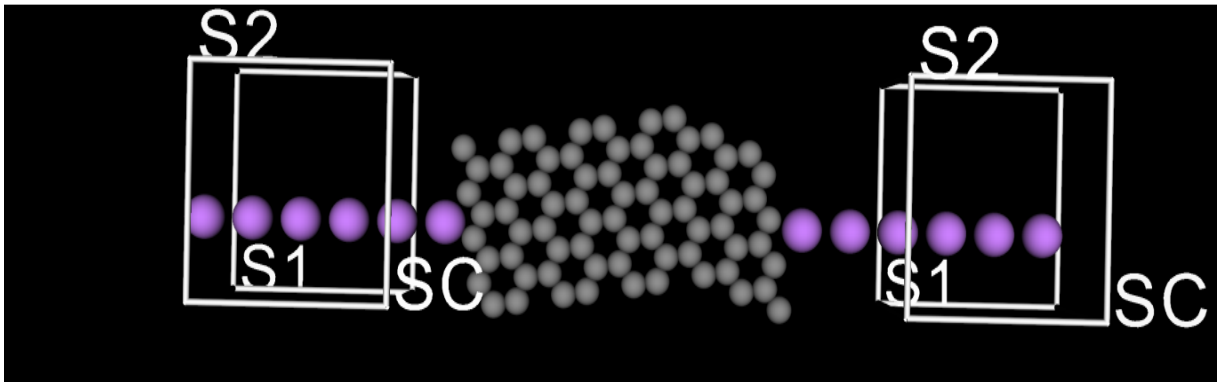

Figure 3.2 (c) Two probe device (D4) in which the central region constitutes of a modeled structure of H-GNR having width of 8 C-atom layers and along length there is a repetition of 6 C-atom unit cells which comprise of AC ribbon on left end and ZZ ribbon on right end.

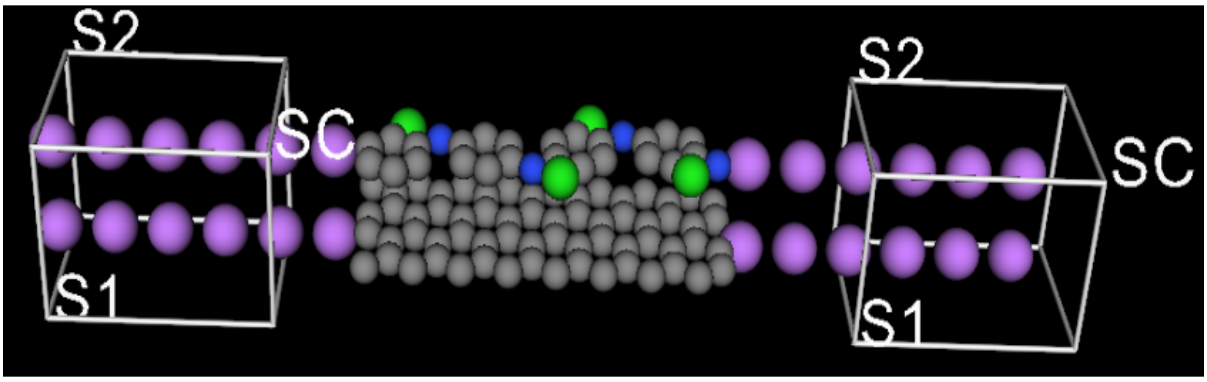

Figure 3.3 Two probe device (D5) in which the central region constitutes of a modeled structure of ZZ-GNR/PAn nanocomposite in parallel conformation in which the ZZ-GNR as shown in the figure 3.2 (a).

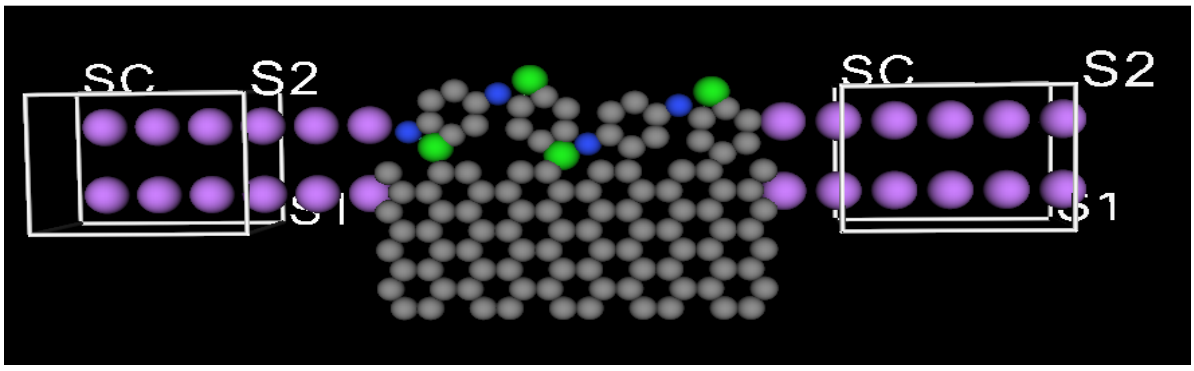

Figure 3.4 Two probe device (D6) in which the central region constitutes of a modeled structure of AC-GNR/PAn nanocomposite in plane conformation in which the AC-GNR as shown in the figure 3.2 (b).

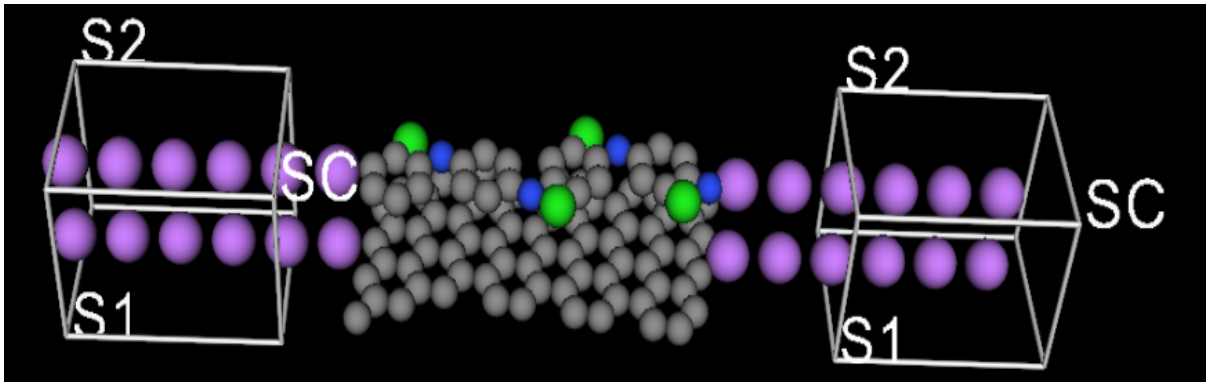

Figure 3.5 Two probe device (D7) in which the central region constitutes of a modeled structure of H-GNR/PAn nanocomposite in parallel conformation in which the H-GNR as shown in the figure 3.2 (c).

In order to carry out the study of the electronic structure and transport properties of the nano-components viz. PAn, ZZGNR, ACGNR, HGNR, and the nano-composites viz. ZZGNR/PAn, ACGNR/PAn and HGNR/PAn both in plane and parallel plane conformations through simulation, a virtual environment in the nanoregime is created to get the calculations of the physical parameters. In which we have performed following sets of simulational experiments-such as Density of States (DOS), Transmission Spectrum (TS), Transmission Coefficient (TC), Total energy (TE), Eigen Value (EV), Eigen States (ESs) and I–V characteristics.

Set 1: Calculation of physical properties of various samples which comprise of components of the photovoltaic nanocomposite like Polyaniline, Zigzag, Armchair and Hybrid graphene nanoribbons using the two probe devices are given in the figures 3.1 and 3.3 (a) to (c).

Set 2: Calculation of physical properties of nanocomposite sample of the zigzag graphene nanoribbon/ polyaniline nanocomposite in parallel plane conformation using the two probe device are given in the figure 3.4.

Set 3: Calculation of physical properties of nanocomposite sample of the armchair graphene nanoribbon/ polyaniline nanocomposite in plane conformation using the two probe device are given in the figure 3.5.

Set 4: Calculation of physical properties of nanocomposite sample of the hybrid graphene nanoribbon/ polyaniline nanocomposite in parallel plane conformation using the two probe device are given in the figure 3.6.

The above four sets of experiments are performed under unbiased condition by the help of the following six basic procedures. At first, we used the molecular builder tool to build a molecule and atomic manipulator tool for setting up two probe systems. In the second step, python scripts of the samples are prepared and loaded/dropped into the nanolanguage scripter. The third step comprises of setting up the parameters for the Density Functional Theory calculation using a method tab in the nanolanguage scripter. For the determination of the DOS, TS, TE, TC, EV, ESs and the basic parameters taken were shown in the table below.

Table 3.3. Basic Parameters used to simulate the different two probe device samples

Basic Parameters Used	**Two probe system**	
Basis set parameters	Type	Single zeta
	Energy shift	0.01 Rydberg
	Delta Rinn	0.8
	V_0	40 Rydberg
	Split Norm	0.15
	Radial Sampling DR	0.001 Bohr
Brillouin zone integration parameters	Number of k-points (A)	1
	Number of k-points (B)	1
	Number of k-points (C)	500
Eigen State Occupation	Left electrode-electron temperature	300 K
	Rightelectrode-electron temperature	300 K
Electrode Voltage	Left Electrode	0 Volt
	Right Electrode	0 Volt
Electron Density	Mesh Cut-off	Central150 Rydberg
Energy Counter integral parameters	Circle Points	30
	Integral lower bound	3 Rydberg
	Fermi Line Points	4
	Real Axis infinitesimal	0.01 eV
	Real Axis Point Density	0.02 eV
Exchange Correlation Functional	LDA.Pz (Perdew–Zunger functional)	
Iteration Control	Tolerance	1e-005
	Criterion	Total Energy
	Maximum Steps	500
Iteration Mixing	Quantity	Hamiltonian
	Diagonal Mixing Parameter	0.1
	Algorithm	Pulay
	History Steps	6
Two center Integral Parameters	Points	1024
	Cut-Off	2500 Rydberg
Two Probe Algorithm Parameters	Electrode Constraint	Off
	Initial Density Type	Equivalent Bulk

Finally, a numerical calculation (.nc) file is created under the self-consistent tab which stores results of each of the iteration step. Under analysis tab of the nanolanguage scripter, we defined the quantities like DOS, TS, TC, TE, EV and ESs. In the fourth step, the path to store the calculated results is given to save the specifications of the entire calculation as a nanolanguage script in a proper folder. The fifth step is an execution step for the nanolanguage script using a DOS command window to calculate the desired results. As the program execution terminated normally, a complete calculation file is obtained from the log window and is stored for the further analysis. This file consists of huge data as it included the initialization parameters, user defined conditions, description about the nanostructure system and the coordinate values with respect to its dimensionality and most importantly the large iterative data of self consistent calculations. The basic idea behind the self consistent calculations is to calculate and compare the output values obtained after such successive iterations. This loop like process repeats continuously unless the difference between the two successive calculations became less than a default set value of accuracy. Sixth step, the .VNL file in which the result is stored, is dragged and dropped in the result browser and a nanoscope. The results DOS, TS, TC and TE are examined in the result browser and EV, ESs are in the nanoscope. For the I–V measurement we have taken the device structures, numerical calculation files of samples with the help of numpy mathematical functions. We have introduced the bias of the value from [-1, 3] V across the devices and we got the values of respective currents from for all the samples, with the help of non-equilibrium green's function (NEGF).

CHAPTER FOUR

4. Results and Discussions

Now we intend to present and discuss the results that we have obtained using Ab initio DFT LDA NEGF simulations on as modeled nano-composite samples. Various calculations for the Density of states (DOS), Transmission Spectrum (TS), energy eigen states (ES) and I-V measurements are performed. A choice of Lithium (Li) linear atomic chains for the electrode material that is used to connect the bias in all of our two probe devices is deliberate and consistent. Because firstly we wish to reduce the computation time and the use of few atom chain as electrical contact is a good option. Secondly these atomic strings are perfectly metallic nanowires [98, 99, 100] which are also even expected to show ballistic conductance up to $3G_0$ values (G_0 being a conductance quanta) owing to their unique strong bonding character. Around a Fermi level, these atomic wires show a band structure that confirms a doubly degenerate π band and σ^* band crossing the Fermi level [101]. As synthesized real graphene nanoribbon/organic semiconductor nanocomposites by various physical or chemical routes often have random distributions. Because in such blended nanomaterials, the nanoribbon is usually aligned spontaneously with a polyaniline in different possible conformations. Two exemplary conformations are one in which the axis of the PAn is aligned parallel to the nanoribbon length either in the same plane or in the two different planes but parallel to each other. Infact the blended GNR-PAn nanocomposites are frustrated systems in which the rate of composite formation far exceeds the natural process of energy minimization. So even in such blended systems, the self-assembly allows a possibility of a presence of the percolating structures owing to the axial alignment of the two components of the composite [102]. The percolation effect induces a number of nanoribbon-PAn composite units to join each other end to end in the form of chain like orientations. The percolatively oriented nanocomposites are also expected to show high conductivity and mobility [103]. Room temperature mobility of the percolatively oriented conducting polymer transistors has already been reported to be as high as $1cm^2/Vs$ [104].

In order to mimic the perfect axial alignment a criteria of convergence for Qausi Newtonian forces used in the geometrical optimization of as modeled nanocomposite structures is not followed in the present work. The only convergence criterion we have used is the total energy for GNR-PAn axially aligned nanostructures. This is a necessary requirement to observe the electronic and transport properties of the aligned nanostructures in the percolation regime.

For the reason that often, the geometrical optimization and nanostructural alignment are competitive processes in the percolating systems.

Table 4.1 Transmission coefficients and total energies of a range of D1 to D7 device samples

S.No	Sample (device) name	Transmission coefficient		Total energy
		0(hole)	1(electron)	
1	D1	0.0266	0.6233	-6642.0637 eV
2	D2	0	0	-10070.5950 eV
3	D3	0.0008	0.0007	-12564.3156 eV
4	D4	0.0005	0.0049	-11305.1591 eV
5	D5	0.0279	0.1793	-16749.3760 eV
6	D6	0.0014	0.2762	-16516.6774eV
7	D7	0.0612	0.1771	-17443.9975 eV

A table 4.1 summarizes the results of transmission coefficients for the hole and electron conduction channels and total energies that is the sum of all the band structure energies for the device D1 to D7 as shown in the figure 3.1 to 3.5.

Following plots sub-sections from 4.1 to 4.7 represent our results of density of states, transmission spectrum, eigenstates-0 corresponding to that of holes in valance band, eigenstates-1 corresponding to that of electrons in the conduction band and I–V characteristic calculations for all of our devices those are schematically depicted from the figures 4.1(a-e) to 4.7(a-e).

4.1 Device D1 with PAn in central region

A plot of the density of States vs energy for the polyaniline is shown in a figure 4.1 (a). The energy range is located from -1 eV to 3 eV. There is an occurrence of sharp peaks in the DOS across -0.39 eV and 0.34 eV and around the Fermi energy level (0 eV). A peak at ~-0.4 eV corresponds to contributing states arise from a π valence band of the organic semiconductor. The other peaks at the upper end of the Fermi level placed in between an energy range of ~0.34 eV to ~2.6 eV can be attributed to a π^* conduction band state and mid gap states induced by the dopant (Cl) in the conjugated conducting chain of PAn. Hence as expected with the addition of

chlorine proximity to the PAn conjugation backbone, the ab-initio DFT-LDA calculations have yielded a DOS spectrum with rich singularity features without any significant contribution to the equilibrium conductivity as shown in the figure 4.1 (a). Hence the materials is in a semiconducting state with a small peak at the Fermi level although decorated with a large number of inter gap states, which will definitely improve the central region's photon absorption for as incident solar light.

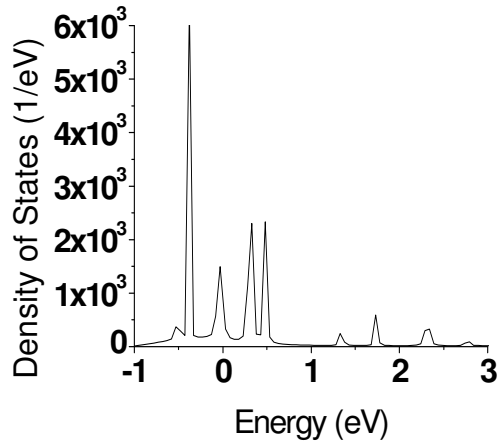

a. Density of States vs energy

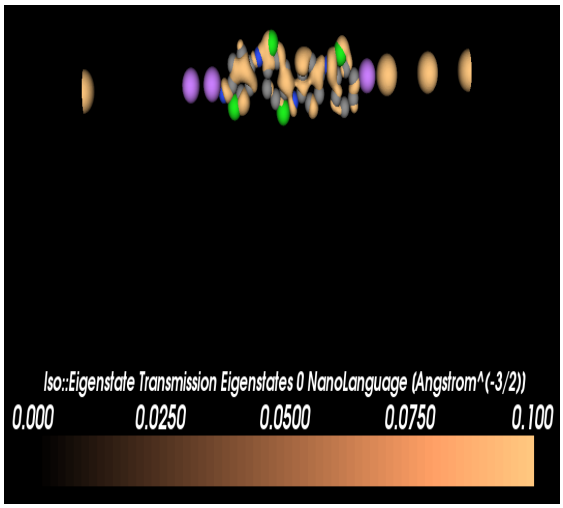

c. Hole Eigen state transmission channel

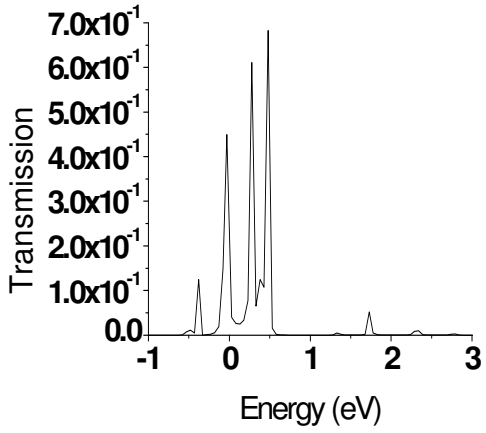

b. Transmission spectrum vs energy

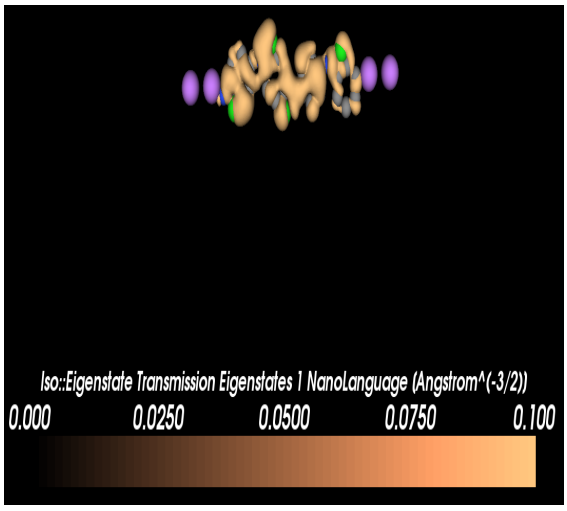

d. Electron Eigen state transmission channel

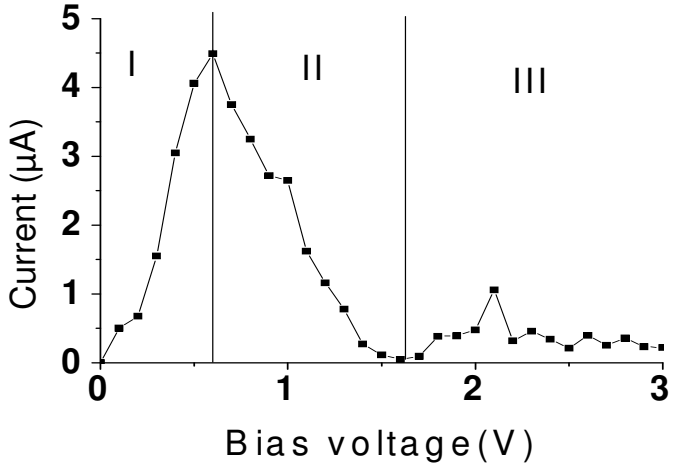

e. I–V characterstics

Figure 4.1 (a-e) Electronic and transport properties of PAn in device D1.

A resonant peak exactly at the zero point of energy spectrum with a significant DOS value of ~1500 is observed. Such resonant features are also earlier reported to be typically found in several two-probe devices and more commonly known as DOS resonance peaks or simply Fano peaks. Very recently, Furst et al [105] have proposed that matching of localized states present in the central region, which is the polyaniline in this modeled device sample, and the contributing states in the electrodes, which are left and right Li-linear atomic chains, is the origin of this Fano symmetry that gives rise to resonant peak at near the Fermi level.

We have also observed a similar transport channel at the Fermi level in our transmission spectra, which is attributed to a presence of the Fano symmetry in this device. However, we are sure that this is not a chlorine dopant induced Fano effect, because the dopants usually interfere their localized states (atomic orbitals of Cl atom) with that of central region (contributing states in polyaniline conjugated backbone) yielding an anti-Fano type of effect or a dip in DOS spectrum near to the E_F [72, 105]. If we look carefully at the DOS spectrum the presence of a lower resonant peak at -0.39 eV closer to Fermi level arises due to hole delocalization in polyaniline which is stronger than the upper resonant peak at 0.34 eV. This effect can only be ascribed to the hole transport character of the as modeled chlorinated polyaniline where π band related hole eigenstate transmission channel is more effective due to sp^2p_z configuration of C-orbitals which overlaps along the length of conjugation [106]. But due to the effect of

chlorination in PAn, we can also see several other resonant peaks at the upper levels. Also, an observance of broader and stronger upper resonant peaks nearer to the Fermi level in the transmission spectrum are signatures of presence of several electron transport channels in this modeled PAn structure [107]. Our observance is also further corroborated from our studies of individually resolved electron and hole Eigen state conduction channels [108] depicted in figures 4.1 (c) and (d). It is clear from the images of the two conduction channels 0 and 1 that both of them are very strong channels but the equivalent conductance of channel (1) is approximately twenty three times more than that of channel (0). The respective values of transmission coefficients at zero bias are given in Table 4. Hence the as modeled structure can effectively behave as an efficient conduit for both the hole and electron transport.

We have further studied a non-equilibrium conductance of the Pan nano-device by applying a bias of -1 to 3 V in between source (left electrode) and drain (right electrode). I–V characteristics of the device are extracted from the values of non equilibrium conductance as described in the section (3.1.4) using the Landauer's relation. As obtained I–V measurement of the polyaniline is shown in a figure 4.1 (e). Clearly, the I–V curve follows some non-ohmic conduction mechanisms, which is typical to all nanostructural materials. This is because of a presence of van Hove singularities in the Density of States of one dimensional nanowires owing to the quantum size confinement effect [109]. The non-ohmicity induced phenomenon of negative differential resistance (NDR), which occurs spontaneously in our result after an ohmic region of 0 to ~ 0.5 V, which is further followed by a plateau of saturated current from ~ 1.5 V onwards. Hence, clearly we have three distinct I–V features (I) nearly ohmic region but with differential conductance, (II) non ohmic region with NDR and (III) current saturation as shown in the figure. A sharp ascend of the current in region (I) is obviously arises from the presence of contributing states due to a number of mid gap states in the chlorinated polyaniline. However, the PAn is also strictly a nanostructure hence most of the upper resonant states as discussed in DOS and transmission spectrums still have only a few numbers of singularities and the conduction channels decays very rapidly after 0.5 V. Hence we observe a true NDR regime of the PAn two probe nanodevice from V>0.5 V until higher energy electron channels comes into this picture at V>1.8 V. Nevertheless there is also a small T(E) channel induced by chlorine proximity related transmission oscillations which gives rise to a small I–V peak at ~ 2 V and a

complete saturation of the current thereafter with a very small aggregate value of charge transport.

4.2 Device D2 with ZZGNR in central region

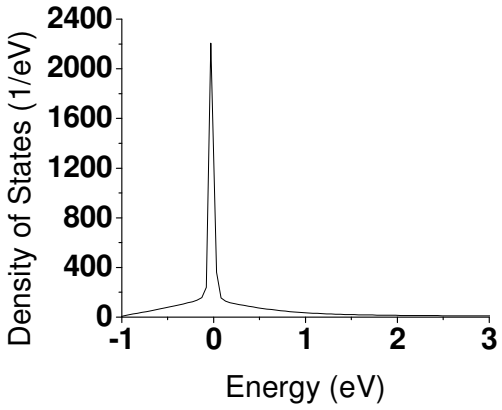

a. Density of States vs energy

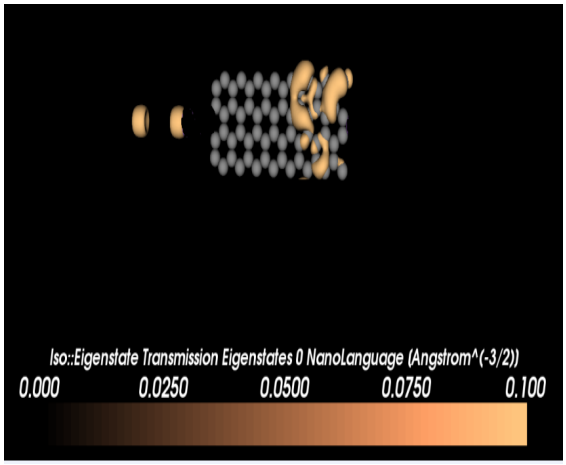

c.Hole Eigen state transmission channel

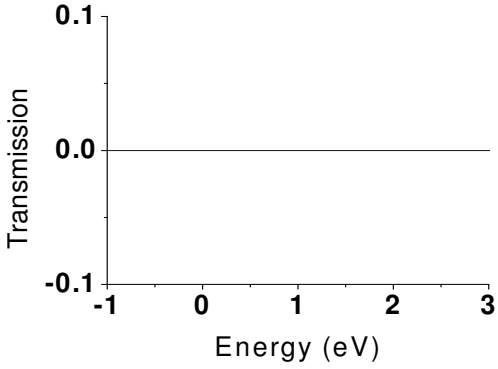

b. Transmission spectrum vs energy

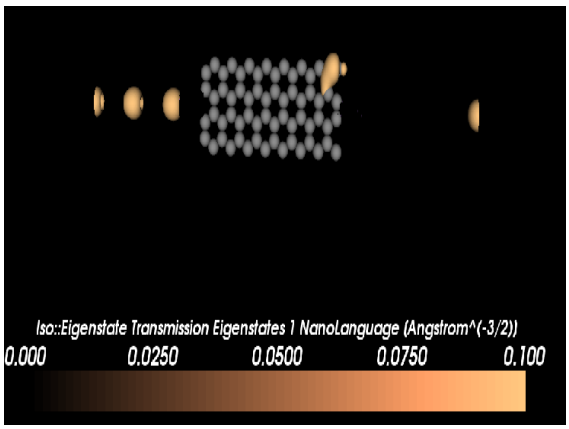

d. Electron Eigen state transmission channel

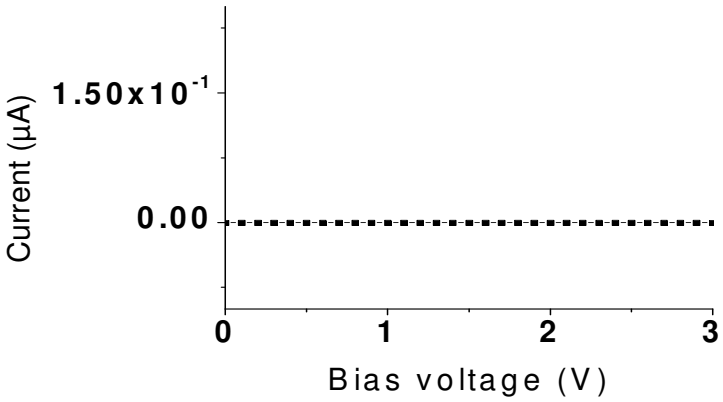

e. I–V characterstics

Figure 4.2 (a-e) Electronic and transport properties of ZZGNR in device D2

A figure 4.2 (a) shows density of States (DOS) of the zigzag graphene nanoribbon under an applied voltage of -1 eV to 3 eV. The infinitely long and sufficiently wide ZZGNRs are supposed to be conductive due to their edge states which provide a through channel for conduction [110]. Usually these ZZGNR edge states are found near the fermi level (at E_F =0, in the energy corrected spectrum) where the mid gap of the material is expected. Hence, the edge states are a good source of equilibrium conductance in ZZGNR, Park et al have reported at least a three 100% eigen channel conduction in ZZGNR for a clear window of ± 0.2 eV around E_F. But the ZZGNR with finite length and small width behaves differently in a two probe device configuration [111]. As we can see from the figure 4.2 (a) there is only a single intense DOS peak centered on E_F in the energy window of -0.13 eV to 0.10 eV. However the intense mid gap peak which is the hall mark of ZZGNR is present in our modeled two probe device but clearly the conductance window is heavily minimized in our simulational experiment. The drastic reduction in ZZGNR's DOS can be attributed to a reduced coupling between the lithium electrodes and the ZZGNR central region which results in the antiresonance effect leading to diminished contributing states of the pristine ZZGNR. Also in low dimensional systems like graphene nanoribbons the charge transport mostly depends upon the quantum transport properties, in which the lowest unoccupied molecular orbital of the central region i.e π^* band of ZZGNR should be perfectly aligned with the conduction band of electrodes for better charge transport [112]. This doesn't seem to the case in our present device sample D2 instead of a very good total energy minimum of -10070.59 eV obtained for this device. Hence the T(E) is almost

flat and negligible without any significant conduction channel, as visible in figures 4.2 (b) to (d). Also as expected the I–V curve of device D2 shows almost zero value of current even for high voltages.

4.3 Device D3 with ACGNR in central region

Amongst ACGNR nanostructures, the edge state kind of conduction channels are absent due to a reduced π-π coupling at the edge and large effective C-neighbor distances in the armchair edge . Thus ACGNRs are inherently semiconducting with direct band gaps [113]. However the band gap of ACGNR changes with respect to width and length of ACGNR. Typically, for the ACGNR of finite length of 6 unit cells, the calculated band gaps are 0.49, 1.034, 0.709, 0.195, 1.433 and 0.29 eVs for corresponding widths of 17, 10, 9, 8, 7 and 5 carbon atoms [114]. A lowest calculated value of E_g is for the 8-ACGNRs while a largest band gap of 1.433 eV is found for the 7-ACGNRs.

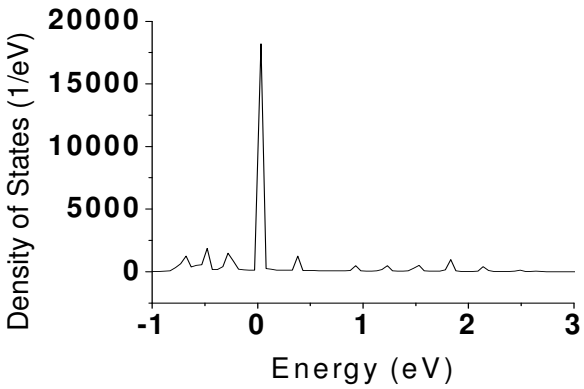

a. Density of States vs energy

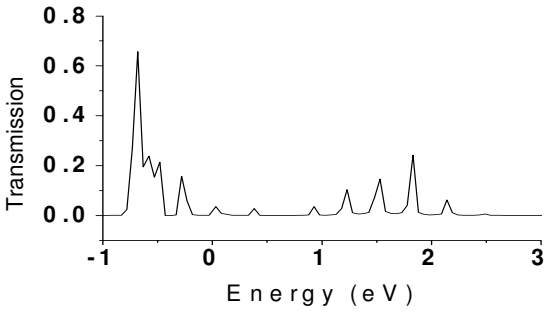

b.Transmission spectrum vs energy

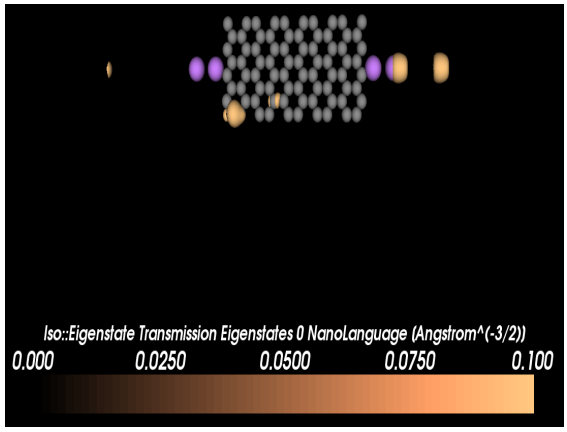

c. Hole Eigen state transmission channel

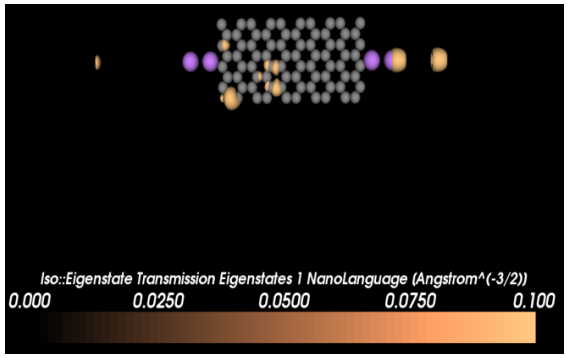

d.Electron Eigen state transmission channel

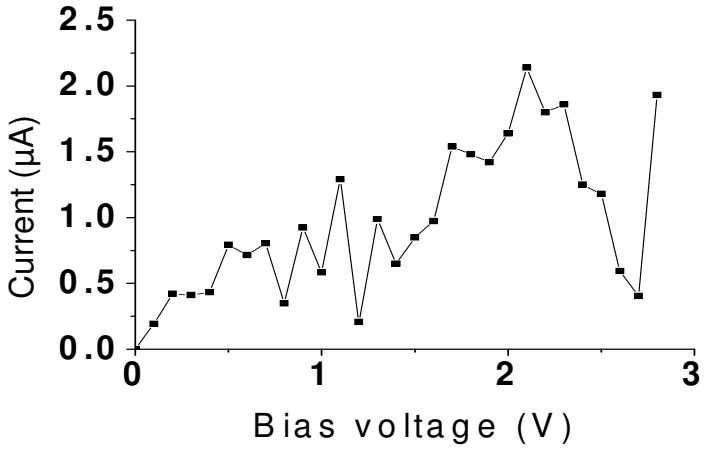

e. I–V characterstics

Figure 4.3 (a-e) Electronic and transport properties of ACGNR in device D3.

In the present study, we have taken a finite length of 5 unit cells and finite width of 8C-atoms in the as modeled ACGNR. Another interesting feature visible very clearly in the ACGNR nanodevice's DOS spectrum is a prominent contributing state peak at the Fermi level which is due to the as described enhanced coupling in between the central and electrode regions of the device and the injection of contributing states from left and right electrode regions to ACGNR. The effect of enhanced coupling is also found in appearance of several resonant states at the upper and lower proximities of the zero point. The upper resonant states are found in an energy window of 0.5 to 2.1 eV while the lower resonant peaks lie just in the lower immediacy of hole delocalization state. Because of the total DOS corresponding to hole contributing states is high, the T(E) shows a broader (hump) channel around the π band peak and this results in higher coefficient of transmission of hole in comparison to that of electron with a value of 8.0 $x10^{-4}$ (refer Table 4). A small continuity in the decomposed eigen state channels for the contributing holes and electrons as shown in figures 4.3 (c) and (d) is due to lower values of the transmission coefficients.

The I–V curve is shown in a figure 4.3 for the ACGNR device, which further explains in a most comprehensive manner, all the ideas that we have generated from DOS/TE/ES study of ACGNR two probe model. On looking carefully there is an incredible rise of the current near +100 mV from the zero bias, which can only be ascribed to the immediately available high electrode-coupled resonant states followed with a small I–V plateau of ~150 mV, which is due to

a decay of these resonant states and an unavailability of any other inter band gap contributing states. Nevertheless, a steady rise of the current is obtained after 0.4 V due to an impact excitation by injected hot electrons to overcome the fundamental energy gap. Although the ACGNR is a strict nano material but a steady rise in the current is obtained up to 2.1 V with some oscillatory kinks in between due to the large coupling extent of external electrodes with the ACGNR. The coupling extent is found to be high and calculated from a charge value of 324.3349e, which is also the total charge on the central region of the device. But as shown in T(E), we do not have any injected resonant peaks after 2.1 V, which causes a triggering of the NDR in the device as the non equilibrium concentration of charge carriers in the central region vanishes in these transmission gaps. This is also depicted in the form of I–V decay from 2.1 V onwards.

4.4 Device D4 with HGNR in central region

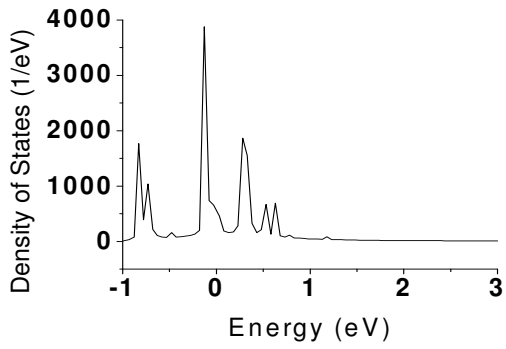

a. Density of State vs energy

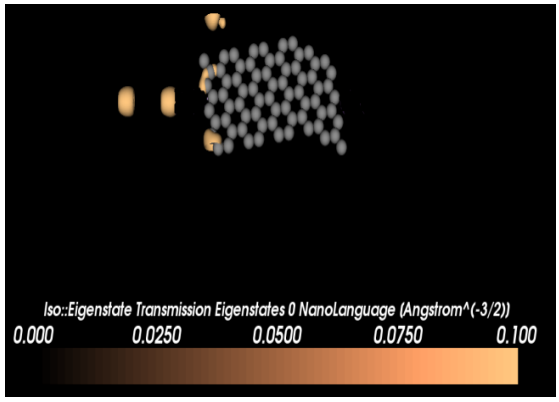

c.Hole Eigen state transmission channel

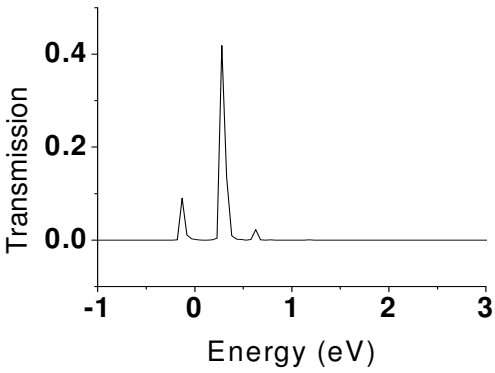

b.Transmission spectrum vs energy

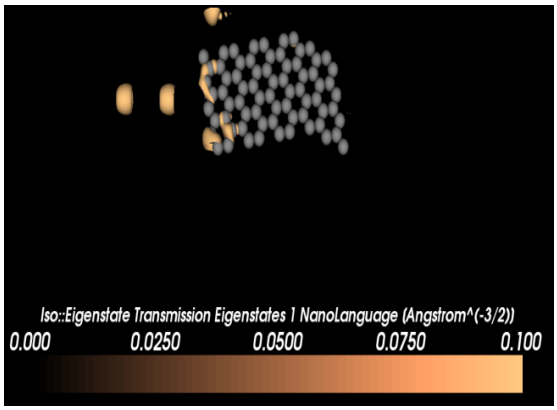

d. Electron Eigen state transmission channel

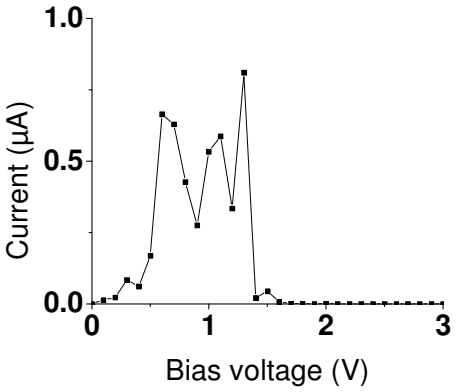

e. I–V characterstics

Figure 4.4 (a-e) Electronic and transport properties of HGNR in device D4.

A plot of DOS vs energy for a system of the hybrid graphene nanoribbon is shown in a figure 4.4 (a). An energy range is set in between -1 to 3 eV. There is an edge in the DOS across -0.72 eV and 0.27 eV around the Fermi level (0 eV) with a total energy gap of 0.99 eV. The DOS is observed due to the zigzag-related $\pi - \pi^*$ band transition. A second prominent DOS features is also observed across -0.83 eV and 0.56 eV with a total energy gap of 1.39 eV that is because of armchair related $\pi - \pi^*$ transition in this hybrid system. In a transmission vs energy curve a similar trend can be observed on account of these two transitions.

Apart from the two fundamental transitions, there are several other resonant peaks as well both in the DOS and the transmission spectrum, which is attributed to the significant coupling between the central and electrode regions. However, for this hybrid ribbon we do not find any signatures of the Fano like coupling. Absence of the Fano states is also visible in a I–V measurement encompassing an initial plateau at zero bias without any sharp rise in the current. Contrary to our earlier expectation about the instability of hybrid structures, we found this sample more stable than the ZZ ribbon, with total energy at -11305.159 eV. However, the stability of the ACGNR sample in the two probe device configuration is found to be largest with a total energy value of -12564.316 eVs. Both the eigen state decomposition channels for this device show small orbital overlaps which are too far from each other with significant discontinuities leading to a large tunneling barrier width and less transmission. The conductivity of this specific sample is found to be small and the I–V characteristics as shown in a figure 4.4

(e) indicate a presence of non-ohmicity in the device. The as measured current becomes almost zero ampere as the bias goes from 0 V to 0.3 V and 1.4 V to 3 V. A stable region of the negative differential resistance (NDR) appears in the I–V characteristics curve of the hybrid graphene nanoribbon. This NDR originates from a transport gap induced by the said selection rule that blocks the electron transition between disconnected energy bands of hybrid graphene nanoribbon.

If we compare all the four singular nanostructures at a glance, the equilibrium contributing states are found to be maximum in the chlorinated PAn due to a stronger coupling in between different components of the device, with a current maximum of the ~5 μA centered around 0.6 V. However, the nano device continues to provide a good high way for charge carriers up to 1.5 V with very high intrinsic hole transport channels. Similarly, among the nanoribbon devices except ZZ ribbon, the devices made up of all other ribbons show good resonant effects and signatures of Fano type coupling are found in all ribbons except for the hybrid ribbon, which would be an interesting topic for further studies. Nevertheless, the ribbon provides excellent highway for electrons, which gives rise to high values of the current maxima in ribbon samples except for the ZZGNR. The maximum current in the ACGNR is ~2.5 μA along a very large bias window of 2 V and ~1.5 μA in the hybrid ribbon with bias window of 0.5 to 1.5 V. Now it will be very interesting to study the two probe device performance of nanocomposite samples of the PAn which are blended with these excellent grapheme nanostructures in the percolating alignment regime. Partly, because of the as expected significant π-π interactions amongst these two C-ring type components of the nanocomposite, a stern divergence in the composite transport properties is anticipated.

4.5 Device D5 with ZZGNR-PAn nanocomposite configured in parallel in the central region.

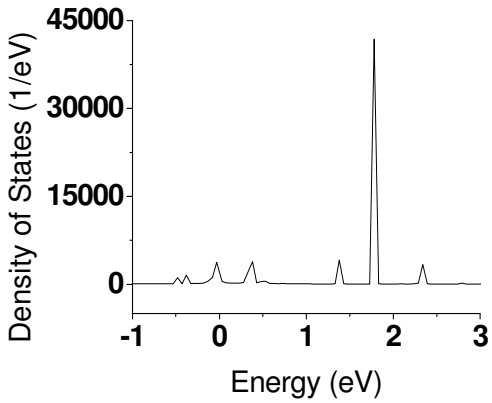

a. Density of state vs energy

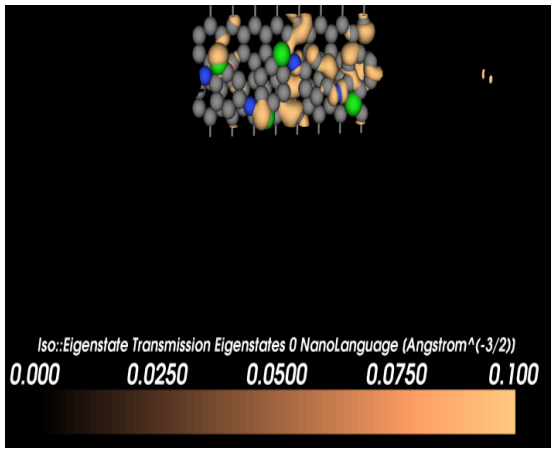

c. Hole Eigen state transmission channel

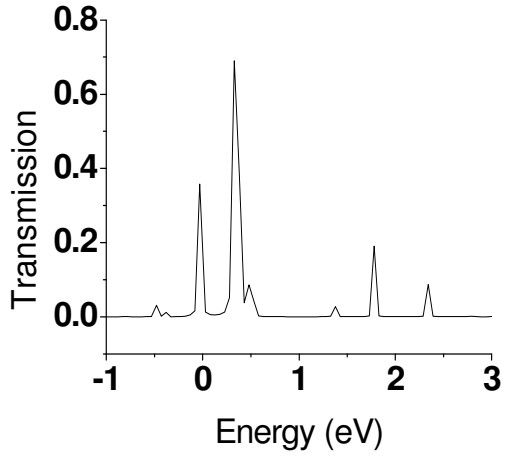

b. Transmission spectrum vs energy

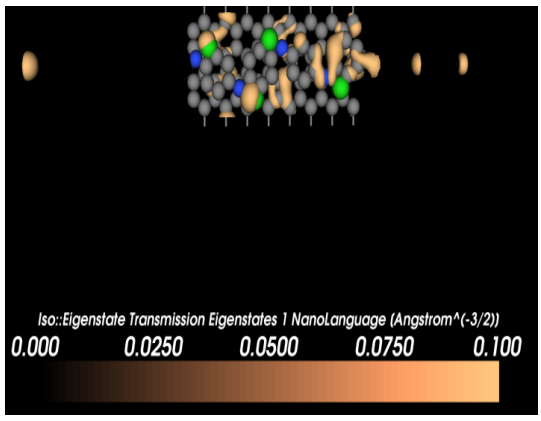

d. Electron Eigen state transmission channel

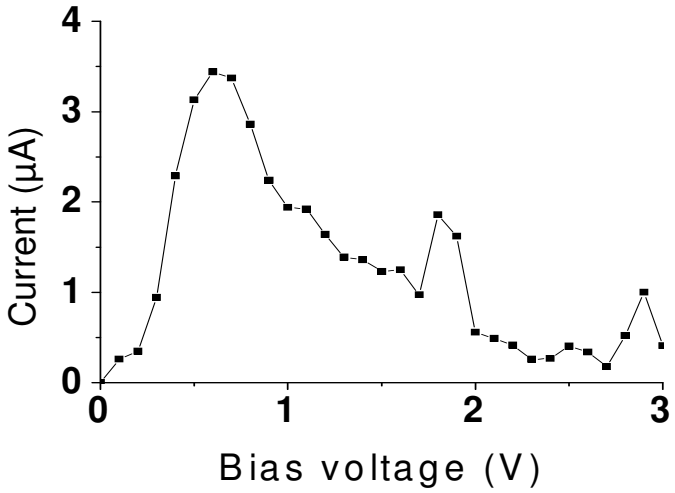

e. I–V characterstics

Figure 4.5 (a-e) Electronic and transport properties of ZZGNR-PAn nanocomposite in device D5

The electronic structure of the nano-device (D5) is clear from a figure 4.5 (a) which is a plot of DOS vs energy for a system of the zigzag graphene nanoribbon blended with the chlorinated polyaniline when they are in parallel conformation. The energy is set in between -1 to 3 eV. In fact a Fano type peak is also observed in ZZ nanocomposite sample which is centered at Fermi level in both DOS and T(E) spectrum. An exceptional resonant state is observed at ~2.0 eV along with several other singularities amid the contributing states. This would obviously give rise to several transmission channels. But the prominent near zero point transmission is from channel 0 for holes and channel 1 for electrons respectively. The transmission channel at ~0.35 eV is strongest due to presence of number of resonant states at upper part of Fermi level. At the same time this nanocomposite device also exhibits some degree of semi-metallicity because the transport channel present at zero point. Hence, the eigen state transmission decomposition for the electron is more continuous as compared to that for the hole delocalized eigen states in figures 4.5 (c) and (d). I–V curve for this sample shows a good steep rise of current commencing from zero finite bias and reaches to its maximum at ~0.65 V. This steepest ascent can be attributed to both the equilibrium contribution states and reemergence of the metallicity in the ZZGNR in the nanocomposite material as well as to resonant modes that exist in the central region owing to the PAn's contributing states injection, further evident from an overlapping eigen state

decomposition. We ascribe the peculiar behavior of this nanocomposite to the significant π-π interactions amongst the two nano components. However, an average NDR regime starts showing up in the I–V after ~0.65 V which continues up to 2 V, with some oscillatory kinks arising from the higher voltage resonant states. Since these discrete resonant DOS states are very high up to ~45,000, therefore there are several NDR regimes in our I–V. Nonetheless, the device performance of ZZGNR-PAn nanocomposites is found to be better than that of the pristine ZZGNR. This implies that there is a strong injection of states among the different components of nanocomposite device at high voltages.

4.6 Device D6 with ACGNR-PAn composite configured in plane in the central region.

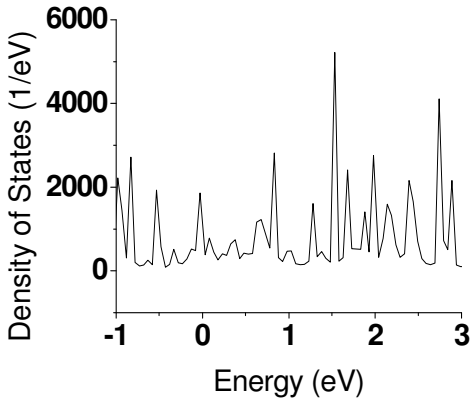

a. Density of state vs energy

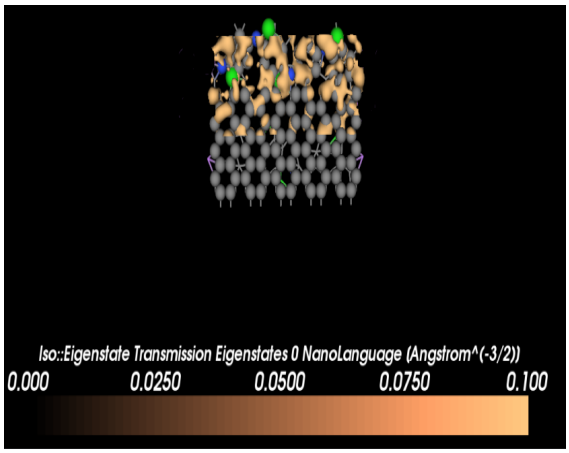

c. Hole Eigen state transmission channel

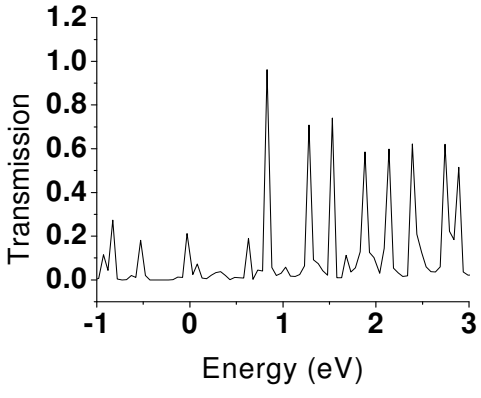

b. Transmission spectrum vs energy

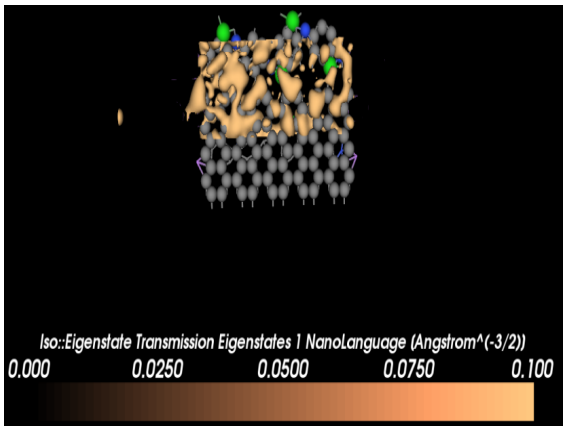

d. Electron Eigen state transmission channel

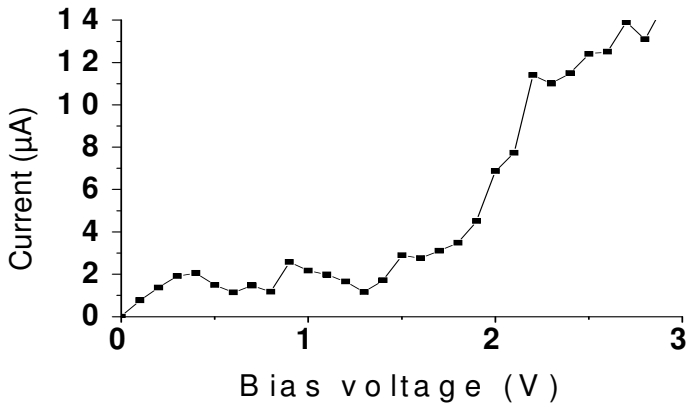

e. I–V characterstics

Figure 4.6 (a-e) Electronic and transport properties of ACGNR/PAn nanocomposite in device D6

The DOS vs energy plot of a armchair graphene nanoribbon with a polyaniline when configured in plane is shown in a figure 4.6 (a), the energy is set from -1 eV to 3 eV. The fact that our pristine ACGNR sample is best coupled with the lithium electrodes among all other samples is also manifested in the form of a number of strong resonant peaks that are found in both DOS and T(E) spectra, which provides a good number of electronic conduction channels in the device. However, there is an asymmetric distribution of contributing states around the Fermi level, which is also an important feature of our ACGNR device (D3) and this minimizes the NDR effect to some extent. From the I–V curve, we can see a continuous rise in the average current with no significant NDR, only the current plateau is found between the voltage values of 0.5 to 1.7 V, after which the current increases steadily. This is an exceptional result which mimics a bulk-like or a pseudo-ohmic character of the nano-device. Because the current increases exponentially after the value of 1.9 V, but at the same time there is a significant value of current at lower voltages. Hence the rectifying behavior cannot be ascribed to the effects of schottky barrier where the leakage current is usually very small. In our case the rectification can be understood from the presence of large number of peaks at higher energies in the DOS and the transmission energy spectra. Also we can see a significant current transport of 14 μA at 2.7 V in this strictly axially aligned nanosystems. By the way, this is the largest value of transport obtained in the present set of studies.

4.7 Device D7 with HGNR-PAn nanocomposite configured in parallel in the central region.

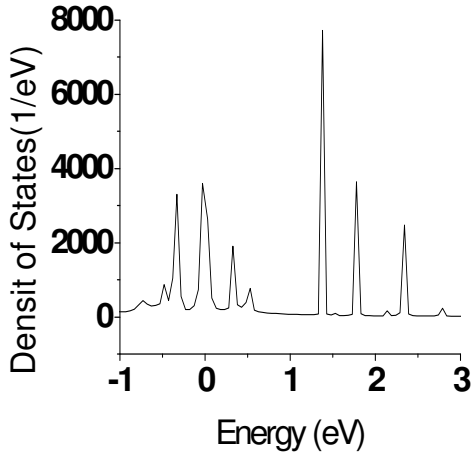

a.Density of states vs energy

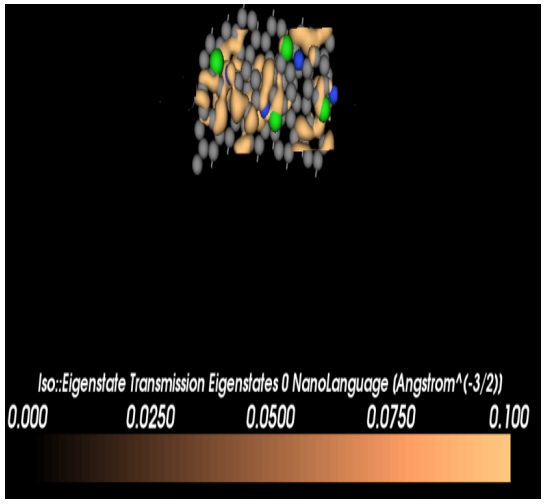

c.Hole Eigen state transmission channel

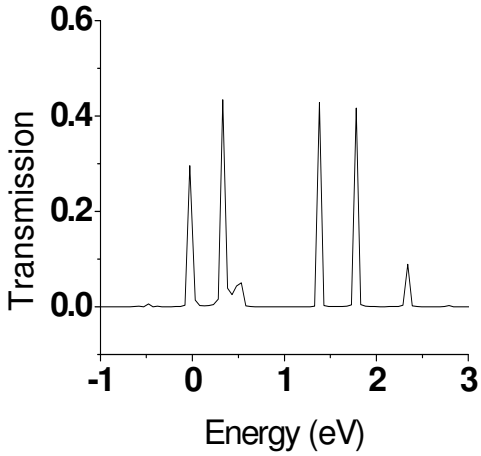

b. Transmission spectrum vs energy

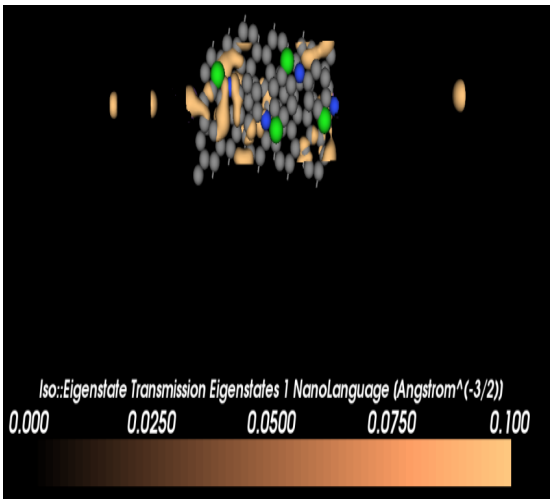

d. Electron Eigen state transmission channel

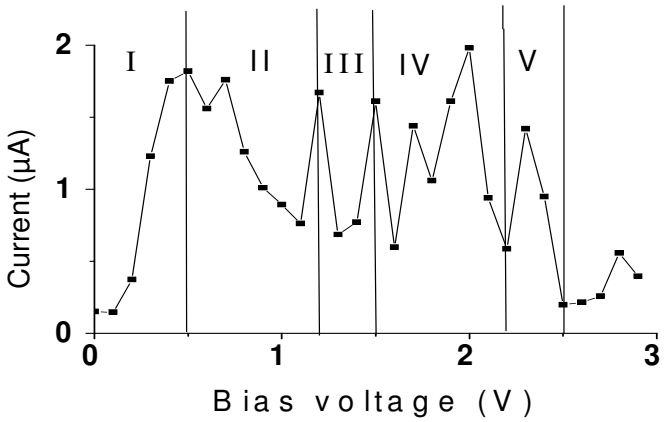

e. I–V characterstics

Figure 4.7 (a-e) Electronic and transport properties of HGNR/PAn nanocomposite in device D7

In DOS vs energy plot as shown in a figure 4.7 (a) the energy is set from -1 eV to 3 eV. There is an occurance of tailing edge effect on both side of the equilibrium peak in the DOS across -0.32 eV and 0.30 eV around the fermilevel (0 eV) which indirectly signifies the extent of coupling in this hybrid nanocomposite. A total energy gap that appears across the fermi energy level is 0.62 eV, along with an equilibrium conduction peak. Nevertheless, this device shows the reduced injection of resonant states from the electrodes. Still the coupling is manifested by strong resonance state at the zero point. Actually, this device is also unique in terms of most of the resonant states are in tens of thousands in number, which ensures well defined strong singular transport channels, yielding several accurate NDR switching regimes. Hence it is easy to predict that these are the ideal characteristics for a high performance nano-switch/nano-transistor that can easily control ultra fast dynamics of modern nanoelectronics owing to high mobilities of respective nano components rather than simply deploying in the nano solar cell technology. However, the device yields a maximum current of ~2 μA among different NDR regimes as depicted in the I–V curve and thus is also useful for the solar cell fabrication along with the D5 and D6 devices. The observation is also evident from the continuous eigen state channels in a figure 4.7. (c) & (d), and the continuous current rise from zero bias up to ~0.5 V. On further increasing the current, secondary NDR regimes originate as shown in I–V measurements in a figure 4.7 (e).

CHAPTER FIVE

5. Conclusion and Future outlooks

5.1 Conclusion

We have studied the electronic structure and transport properties of nanodevices of chlorinated polyaniline (PAn), graphene nanoribbons (GNR) in various edge-conformations and GNR-PAn nanocomposites in-plane and in-parallel alignment device configurations for the very purpose of their deployment as nano-composite active layers in a bulk heterojunction (BHJ) solar cell for smart light harvesting. From the decomposed transport eigen-state channels, as chlorinated PAn is found to be an efficient transport channel with noticeable values of equilibrium conductance. From the DOS and the transmission energy spectra we have found an existence of a number of energy inter-gap states along with fundamental transition states that varies in the energy regime of 0.4 to 3.2 eV which well corresponds to a complete scale of UV-Vis-IR energies. We deem that such a rich electronic band structure of the chlorinated PAn will indeed be helpful for the efficient photon harvesting in the full solar energy spectrum. We also found that all the transport channel corresponding to these energy states are active along with sufficient electronic transmission near the Fermi energy. Such a behavior of the modeled donor material is ascribed to the proximity of a Chlorine atom with the PAn conjugated backbone. The equilibrium conduction states are also found in Graphene nanoribbons 2-probe devices with edge-conformations of zigzag, armchair and hybrid forms. Studies of DOS(E) and T(E) spectra of nano-devices indicate a higher number of contributing mid gap states and site selective transport channels, which also reveal the rationale of deployment of these GL-PAn nanocomposite in the BHJ type nano solar cells. The three best nanocomposite samples with excellent charge transport characterstics are particularly found to be suitable for the photovoltaic applications and they comprise of (a) the ZZGNR/PAn composite when configured in parallel, (b) the ACGNR/PAn composite when configured in the same plane and (c) the HGNR/PAn composite when configured in parallel. All the short listed samples show high charge transfer values in their respective transport channels along with significant density of states in the energy range of photovoltaic interest (0 eV to 3 eV). These results also corroborate the obvious higher solar power yield excitations from the GNR-PAn solar cell device.

Another interesting aspect of the present studies is that we have found a rich singularity blueprints in our ab-initio simulations for most of the nanostructures. A phenomenon of negative differential resistance (NDR) is quite often observed during our simulation process, which we have verified rigorously. It is interesting to note that the novel quantum features in our samples could be attributed to the presence of singularities in the density of states and transmission spectrum. However, small peaks in the DOS and the T(E) can be easily ascribed either to the presence of Fano like modes of resonances near the Fermi level or due to the enhance coupling in between the electrodes and the central region of the device in our samples. The NDR is also effortlessly observed in our most I–V measurements. However, we do not observe any significant rectification in our devices either due to the strong coupling/Fano induced conduction modes or due to the pointed nature of DOS features leading to a rapid decay of the current. Observance of significant electronic transmission values near the Fermi level still ambiguous in nature. We have also found the effect of the nanocomposite samples showing severe divergence from the respective physical properties of the individual components, we have attributed such an adherence to the significant π-π interaction amongst the C-ring constituents of the nanocomposite. Nevertheless, in the device D6 a different type of rectification is found in the I–V characteristics that is attributed to the presence of higher energy electronic states in transmission. Needless to say that the work performed in this thesis is of high importance for the optimization of nano OPV solar cell fabrication and its functioning.

5.2 Future outlooks

1. Effect of different cationic/anion dopants on the equilibrium charge transfer through as modeled PAn two probe device.
2. To study the nanoswitch transistor in the device (D7) by Eigen state channel decomposition in various NDR regimes for better understanding of active transport channels.
3. Absence of the Fano effect or the strong LCR coupling in the pristine hybrid nanoribbon systems needs further investigations.

References

1. Zhenga Z., Dua Y., Fenga Q., Wanga Z. and Wanga C., Journal of Molecular Catalysis A: Chemical, 353 (2012) 80.
2. Khan J.M., Kurchania R. and Sethi V.K., Thin Solid Films, 519 (2010) 1059.
3. Yan J., Wei T., Shao B., Fan Z., Qian W., Zhang M. and Wei F., Carbon, 48 (2010) 487.
4. Wang D.W., Li F., Zhao J.P., Ren W.C., Chen Z.G., Tan J., Wu Z.S., Gentle I., Lu G.Q., and Cheng H.M., American Chemical Society Nano, 3 (2009) 1745.
5. Xu Y., Zhao L., Bai H., Hong W., Li C. and Shi G., Journal of American Chemical Society, 130 (2008) 5856.
6. Sun Y., Wilson S.R., and Schuster D.I., Journal of American Chemical Society, 123 (2001) 5348.
7. Zhang X.–F. and Xi Q., Carbon, 49 (2011) 3842.
8. Bhattacharya A. and De A., Progress Solid State Chemistry, 24 (1996) 141.
9. Kalowekamo J. and Baker E., Solar Energy, 83 (2009) 1224.
10. Bube R.H., Photovoltaic Materials: Properties of Semiconductor Materials, Imperial College Press, USA (1998) pp. 1–6.
11. Ong P.–L. and Levitsky I.A., Energies, 3 (2010) 313.
12. Gomard G., Drouard E., Letartre X., Meng X., Kaminski A., Fave A., Lemiti M., Garcia-Caurel E. and Seassal C., Journal of Applied Physics, 108 (2010) 123102.
13. Kippelen B. and Bredas J.–L., Energy Environment Science, 2 (2009) 251.
14. Green M.A., Progress in Photovoltaics: Research and Applications, 9 (2001) 123.
15. Li J., Liu J., Gao C., and Chen G., International Journal of Photo energy, 201 (2011) 1.
16. Kang M.–G., Joon P.H., Hyun A.S., Xu T., and Jay G.L., Journal of Selected Topics in Quantum Electronic, 16 (2010) 1807.
17. Kim Y.H., Sachse C., Machala M.L., May C., Lars M.–M., and Leo K., Advanced Functional Materials, 21 (2011) 1076.
18. Senthilkumar N., Kang H.–S., Park D.–W. and Choe Y., Journal of Macromolecular Science, Part A: Pure and Applied Chemistry, 47 (2010) 484.
19. Nicholson P.G. and Castro F.A., Nanotechnology, 21 (2010) 1.
20. Burkhard G.F., Hoke E.T., Scully S.R. and McGehee M.D., Nano Letters, 9 (2009) 4037.

21. Xue J., Polymer Reviews, 50 (2010) 411.

22. Bernede J.C., Journal of the Chilean *Chemical Society,* 53 (2008) 1549.

23. Cheknane A., Aernouts T. and Merad B.M., Revue Des Energies Renouvelables, 07 (2007) 83.

24. Shrotriya V., Li G., Yao Y., Moriarty T., Emery K. and Yang Y., Advanced Functional Materials, 16 (2006) 2016.

25. Benanti T.L. and Venkataraman D., Photosynthesis Research, 87 (2006) 73.

26. Morita S., Zakhidov A.A. and Yashino K., Solid State Communication, 82 (1992) 249.

27. Sariciftic N.S, Smilowitz L., Heeger A.J. and Wudl F., Science, 258 (1992) 1474.

28. Coakley K.M., and McGehee M.D., Chemistry of Materials, 16 (2004) 4533.

29. Chiang C.K., Fincher C.R., Park Y.W., Heeger A.J., Shirakaw H., Louis E.J., Gau S.C., and Macdiarmid G.A., Physical Review Letters, 39 (1977) 1098.

30. Rimbu G.A., Stamatin I., Jackson C.L. and Scott K., Journal of Optoelectronics and Advanced Materials, 8 (2006) 670.

31. Epstein A.J. and Jiang Y., US Patent, 5 (1999) 164.

32. Patil S.D., Raghavendra S.C., revansiddappa M., Narsimha and Prasad N.A., Bulletin of Materials Science, 30 (2007) 89.

33. Huyen D.N., Tung N.T., Thien N.D., and Thanh L.H., Sensors, 11 (2011) 1924.

34. Sajeev U.S., Mathai C.J., Saravanan S., Ashokan R.R., Venkatachalam S. and Anantharaman M.R., Bulletin of Materials Science, 29 (2006) 159.

35. Afzal A.B., Akhtar M.J., Nadeem M., Ahmad M., Hassan M.M., Yasin T., and Mehmood M., Journal of Physics D: Applied Physics, 42 (2009) 1.

36. Sordo J.A., Varela-Alvarez A., Scuseria G.E., Journal of American Chemical Society, 127 (2005) 11318.

37. Gospodinova N. and Terlemezyan L., Progress of Polymer Science, 23 (1998) 1443.

38. Ansari A.A., Khan M.A.M., Khan M.N., Alrokayan S.A., Alsalhi M.S., Journal of Semiconductors, 32 (2011) 043001.

39. Stejskal J., Pure Applied Chemistry, 5 (2002) 857.

40. Yakuphanoglu F., Basaran B., Senkal B.F. and Sezer E., Journal of Physical Chemistry B, 110 (2006) 16908.

41. Mishra A.K. and Tandon P., Journal of Physical Chemistry B, 113 (2009) 9702.

42. Parsa A., Hosseini S.H. and Asefoddoleh M., European Journal of Scientific Research, 26 (2009) 369.

43. Lee M.H., Speyer G. and Sankey O.F., Journal of Physics: Condensed Matter, 19 (2007) 1.

44. Elsayed A.H. , Mohy Eldin M.S., Elsyed A.M., Abo Elazm A.H., Younes E.M. and Motaweh H.A., Journal of Electrochemistry Science, 6 (2011) 206.

45. Kurmaev E.Z., Katsnelson M.I., Moewes A., Magnuson M., Guo J.–H., Butorin S.M., Nordgren J., Ederer D.L. and Iwami M., Journal of Physics Condensed Matter, 13 (2011) 3907.

46. Chipara M., Aldicaa G., Huib D., Dimoniec M., Laud K.T., Georgescue L. and Munteanue I., Journal of Optoelectronics and Advanced Materials, 6 (2004) 297.

47. Neto Castro A.H., Guinea F., Peres R.N.M., Novoselov K.S. and Geim A.K., Reviews of Modern Physics, 81 (2009) 109.

48. Verdejo R., Bernal M.M., Romasanta L.J. and Lopez–Manchado M.A., Journal of Materials Chemistry, 21 (2007) 3301.

49. Hu Y.H, Wang H., and Hu B., Chemistry and Sustainability, 3 (2010) 782.

50. Sun Y., Wu Q. and Shi G., Energy and Environment Science, 4 (2011) 1113.

51. Zhu Y., Murali S., Cai W., Li X., Suk J.W., Potts J.R. and Ruoff R.S., Advanced Materials, 22 (2010) 3906.

52. Fan X.–Y., Nouchi R., Yin L.–C. and Tanigaki K., Nanotechnology, 21 (2010) 1.

53. Mazher J. and Shukla A., US Patent, 3 (2007) 0236706.

54. Pumera M., Chemical Society Review, 39 (2010) 4146.

55. Shahoo S. , Indian Journal of Pure and Applied Physics, 49 (2011) 367.

56. Lin Y.–M., Perebeinos V., Chen Z., and Avouris P., Physical Review B, 78 (2008) 161409.

57. Ozyilmaz B., Jarillo–Herrero P., Efetov D., Abanin D.A., Levitov L.S. and Kim P., Physical Review Letters, 99 (2007) 166804.

58. Zwierzycki M. and Krompiewski S., Acta Physica Polonica A, 118 (2010) 856.

59. Padilha J.E., Pontes R.B., Da Silva A.J.R. and Fazzio A., International Journal of Quantum Chemistry, 111 (2011) 1379.

60. Faccio R., Denis P.A., Pardo H., Goyenola C. and Mombrú Á.W., Journal of Physics: Condensed Matter, 21 (2009) 1.

61. Jiao L., Wang X., Diankov G., Wang H. and Dai H., Letters of Nanotechnology, 5 (2010) 321.

62. Kharche N., Zhou Y., O'Brien K. P., Kar S. and Nayak S. K., ACS Nano, 5 (2011) 6096.

63. Nakada K., Fujita M., Dresselhaus G. and Dresselhaus M.S., Physical Review B, 54 (1996) 17954.

64. Satller K.D., Handbook of Nanophysics: Functional Nanomaterials, John Wiley & Sons Ltd, Chichester (2011) pp. 328–466.

65. Abadir G.B., Walus K. and Pulfrey D.L., Nanotechnology, 21 (2010) 1.

66. Rosenkranz N., Mohr M. and Thomsen C., Annals of Physics, 523 (2011) 137.

67. Dutta S. and Pati S.K., Journal of Materials Chemistry, 20 (2011) 8207.

68. Yazyev O.V., Capaz R.B. and Louie S.G., Physical Review B, 84 (2011) 1.

69. Tao C., Jiao L., Yazyev O.V., Chen Y.–C., Feng J., Zhang X., Capaz R.B., Tour J.M., Zettl A., Louie S.G., Dai H. and Crommie M.F., Nature Physics, 1038 (2011) 1.

70. Zhou X., Wu T., Hu B., Yang G. and Han B., Chemical Communications, 46 (2010) 3663.

71. Babić B. and Schönenberger C., Reprint of Corrected Article Physical Review B, 70 (2004) 195408.

72. Fano U., Physical Review, 124 (1961) 1866.

73. Shi X., Dai Z. and Zeng Z., Physical review B, 76 (2007) 235412.

74. Miroshnichenko A.E., Flach S., and Kivshar Y.S., Reviews of Modern Physics, 8 (2010) 2257.

75. Nitzan A. and Ratner M.A., Science, 300 (2003) 1384.

76. Dai Z.X., Shi X.Q., Zheng X.H., Wang X.L and Zeng Z., Physical Review B, 75 (2007) 155402.

77. Lee Y.J., Brandbyge M., Puska M.J., Taylor J., Stokbro K., and Nieminen R.M., Physical Review B, 69 (2004) 125409.

78. Li Y., Yao J., Liu C. and Yang C., Journal of Molecular Structure: Theochem, 867 (2008) 59.

79. Le Rouzo J., Ribet-Mohamed I., Guérineau N., Haïdar R., Tauvy M., Rosencher E., and Chuang S.L., Applied Physical Letter, 88 (2006) 091117.

80. Sun Y.J, Souma S., Li W.J., Zhu X.G, Wang G., Chen X., Ma X.C., Xue Q.K, Jia J.F, Takahashi T. and Sakurai T., Nano Research, 3 (2010) 800.

81. Kemerink M., Koenraad P.M. and Wolter J.H, Physical Review B, 54 (1996-I) 10644.

82. Waser R., Nanoelectronics and Information Technology: Advanced Electronic Materials and Novel Devices, John Wiley & Sons Ltd, Chichester, (2005) pp. 97–99.

83. Engel E. and Dreizler R.M., Density Functional Theory: Theoretical and Mathematical physics, Springer, New York (2010) pp. 1–217.

84. Cramer C.J., Essentials of Computational Chemistry: Theories and Models, John Wiley & Sons Ltd, England, (2004) pp. 249–294.

85. Filippi C., Umrigar C.J. and Taut M., Journal of Physical Chemistry, 100 (1994) 1291.

86. Kohn W., Becke A.D. and Parr R.G., Journal of Physical Chemistry, 100 (1996) 12974.

87. Sholl D.S. and Steckel J.A., Density Functional Theory: A practical Theory, John Wiley & Sons Ltd, New Jersey, (2009) pp. 1–30.

88. Ao Z.M. and Jiang Q., Open Nanoscience Journal, 3 (2009) 34.

89. Bartlett R.J., Lotrich V.F., and Schweigert I.V., Journal of Chemical Physics, 123 (2005) 062205.

90. Pecchia A., Penazzi G., Salvucci L. and Carlo A.D., New Journal of Physics, 10 (2008) 1.

91. Sankar P.A.W. and Kumar K.U., European Journal of Scientific Research, 60 (2011) 342.

92. Yang Z., Wen B., Melnik R., Yao S., and Li T., Applied Physics Letter, 95 (2009) 1.

93. User's Guide SIESTA (October 5, 2009) pp. 89–90.
URL address: www.icmab.es/siesta–joomal/manuales/siesta–trunk–301

94. Summerfied M., Programming in Python 3: A Complete Introduction to Python Language, Addison–Wesley, Boston (2010) pp. 1–12.

95. Phillips D., Python 3 Object Oriented Programming, Packt, Mumbai (2010) pp. 32–192.

96. Guido V.R. and Fred L.D., An Introduction to Python–The Python Tutorials (version 3.2), Springer, New York (2011) pp.1–6.

97. User's Guide-S I E S T A 3.0-beta-15 (March 18, 2010) pp. 5–70.
URL address: www.icmab.es/siesta–joomal/manuales/siesta–trunk–3.0–b.

98. Han Q., Cao B., Zhou L., Zhang G., and Liu Z., Journal of Physical Chemistry C, 115 (2011) 3447.

99. Larade B., Taylor J., Mehrez H., and Guo H., Physical Review B, 64 (2001) 075420.

100. Mozos J.–L., Wan C.C., and Taraschi G., Physical Review B, 56 (1997) 4351.

101. Lang N. D. and Avouris P., Physical Review Letter, 84 (2000) 358.

102. Stauffer D. and Aharony A., Introduction to Percolation Theory, Taylor and Francis, London (1992) pp. 1–6.

103. Osaka I., Zhang R., Sauvé G., Smilgies D.M., Kowalewski T. and McCullough R. D., J*ournal American Chemical Society,* 131 (2009) 2521.

104. Hamadani B.H. and Gundlach D.J., Applied physics letters, **91** (2007) 243512.

105. Fürst J.A., Brandbyge M., Jauho A.–P., and Stokbro K., Physical Review B, 78 (2008) 195405.

106. Pauling L., Journal of the American Chemical Society, 53 (1931) 1367.

107. Brown P.J., Thomas D.S., Köhle A., Wilson J.S., Kim J.–S., Ramsdale C.M., Sirringhaus H. and Friend R.H., Physical Review B, 67 (2003) 064203.

108. Brandbyge M., Sorensen M.R., and Jacobsen K.W., Physical Review B, 56 (1997) 14956.

109. Raquet B., Goiran M., NègreN., Léotin J., Aronzon B., Rylkov V. and Meilikhov E.,, Physical Review B 62 (2000), 17144.

110. Park J., Yang H., Park K. S. and Lee E.–K., Journal of Chemical Physics, 130 (2009) 214103.

111. Cheraghchi H. and Esmailzade H., Physical Review B, 78 (2008) 085123.

112. Taylor J., Guo H., and Wang J., Physical Review B, 63 (2001) 121104.

113. Son Y.–W., Cohen M.L. and Louie S.G., Physical Review Letters, 97 (2006) 216803.

114. Kosynkin D.V, Higginbotham A.L., Sinitskii A., Lomeda J.R., Dimiev A., Price B.K. and Tour J.M., Nature, 458 (2009) 872.